

ASTL.CLS 01.06.12

## X-ray line formation in the spectrum of SS 433

I.I. Khabibullin <sup>\*1</sup>, S.Yu. Sazonov <sup>1</sup>

Received Dec. 2, 2011

**Abstract** — The mechanisms for the formation of X-ray lines in the spectrum of SS 433 are investigated by taking into account the radiative transfer inside the jets. The results of Monte Carlo numerical simulations are presented. The effect of a decrease in line intensity due to scattering inside the jet turns out to be pronounced, but it does not exceed 60 % in magnitude on the entire grid of parameters. The line broadening due to scattering, nutational motion, and the contribution of satellites can lead to overestimates of the jet opening angle  $\Theta$  from the line widths in Chandra X-ray observations. The fine structure of the lines turns out to be very sensitive to the scattering effects. This makes its investigation by planned X-ray observatories equipped with high-resolution spectrometers (primarily Astro-H) a powerful tool for diagnosing the parameters of the jets in SS 433.

Key words: *close binary systems, X-ray lines.*

## 1 INTRODUCTION

The Galactic source SS 433 is currently the only close X-ray binary system observed in a permanently supercritical regime of accretion. This manifests itself most clearly in the presence of a pair of oppositely directed relativistic jets oriented perpendicular to the plane of a supercritical accretion disk (for a review, see Fabrika (2004)).

X-ray observations of the system show that apart from the continuum component attributable mainly to bremsstrahlung from the jets, its spectrum exhibits numerous lines of highly ionized atoms of heavy elements. By measuring their characteristics, one can get an idea of the physical conditions in the regions closest to the compact object in which the jets are formed, accelerated, and collimated (Kotani et al. 1996).

Substantial progress in understanding these fundamental mechanisms has been achieved in the last ten years through observations by the Chandra (Marshall et al. 2002; Namiki et al. 2003; Lopez et al. 2006), XMM-Newton (Brinkmann et al. 2005), INTEGRAL (Cherepashchuk et al. 2005), RXTE (Filippova et al. 2006), and Suzaku (Kubota et al. 2010) X-ray observatories in the standard and hard spectral ranges. However, the uncertainty in physical parameters of the jets (density, size, and opening angle) remains significant (for more details, see Sections 4.3 and 6). With high-spectral resolution instruments (primarily Chandra HETGS), it has been possible to measure the line widths and intensities and to estimate the opening angle, density, and temperature of the hottest parts of the jets from them (Marshall et al. (2002), Namiki et al. (2003), Lopez et al. (2006)). However, these required correcting the previously

adopted standard jet model (Kotani et al. 1996). For example, the emission measure of the hottest parts of the jet estimated from the line intensity in the high-energy part of the spectrum turned out to be approximately half the value expected from the standard model. In addition, it was required to assume an overabundance (about 30% relative to the solar value) of iron, sulfur, silicon, magnesium, and neon (Marshall et al. 2002) for the observed continuum to agree with that predicted from the line intensities. The EPIC/XMM-Newton spectra point to a more than eightfold excess of radiation near the  $K_\alpha$  triplet of helium-like nickel (Brinkmann et al. (2005), Medvedev, Fabrika (2010)). The physical interpretation of such discrepancies was often reduced basically either to the uniqueness of the SS 433 phenomenon or to the inclusion of additional emitting or absorbing components of the system while restricting oneself to using a very simple scenario for the formation of X-ray lines.

In this paper, we study in detail the influence of scattering effects inside the jets on the spectrum of emergent radiation in lines of the standard X-ray band for the first time. The necessity of such a study follows from simple estimates of the jet transverse optical depth for Thomson scattering ( $\sim 0.1$ ) and, what is especially important, for resonant scattering on electron transitions in highly ionized atoms of heavy elements ( $\sim 100$  for the permitted  $K_\alpha$  transitions in helium-like ions). As a consequence, the effect of an increase in the mean free path of a photon before its escape from the jet due to multiple resonant scatterings becomes important. This, in turn, leads to an increase in the probability of being scattered by a “hot” electron and leaving the line while reducing its intensity and forming broad wings.

Using the Monte Carlo technique for radiative transfer

<sup>\*</sup>E-mail: khabibullin@iki.rssi.ru

problems developed by Pozdnyakov et al. (1983) allowed the formation of X-ray lines in the spectrum of the jets to be simulated most accurately by taking into account the multiplicity of the most important of them and the possible deviations from the coronal approximation. As a result, we made predictions regarding the observational line characteristics, bearing in mind the high resolution of planned spectroscopic experiments (primarily Astro-H; see, e.g., Takahashi et al. (2010).

## 2 THE JET MODEL

The standard multitemperature jet model for SS 433 (Kotani et al. 1996; Marshall et al. 2002) served as a starting point for our study. In this model, the X-ray jet is treated as a highly collimated (an opening angle  $\Theta \sim 1^\circ$ ) ballistic plasma flow directed away from the compact object perpendicular to the plane of a supercritical accretion disk. The velocity component parallel to the jet axis is constant at each point and equal to  $0.26c$ . The matter is distributed uniformly within each layer perpendicular to the jet axis. Under the assumption of an axisymmetric flow pattern, it is convenient to introduce a conical coordinate system  $\vec{r}(r, \theta)$ , where  $r$  is the distance measured from the cone vertex along the jet axis and  $\theta$  is the angular displacement from the axis. The directly observable jet region closest to the compact object will be called the jet base. The location  $r_0$ , electron density  $n_{e0}$ , and temperature  $T_0$  of this region as well as the opening angle  $\Theta^*$  are the input parameters of the model.

Given the uniformity of the matter distribution in the  $r = \text{const}$  layer, the law of change of the electron density follows from the condition for the conservation of mass flux along the jet:

$$n_e = n_{e0} \left( \frac{r}{r_0} \right)^{-2}. \quad (1)$$

Using the derived density profile, we can write the thermal balance equation as

$$\frac{dT}{dr} = -2(\gamma - 1) \frac{T}{r} - \frac{2n_e n_i}{3(n_e + n_i)} \frac{\Lambda(T)}{v}, \quad (2)$$

where the first and second terms on the righthand side correspond to the cooling through adiabatic expansion and the losses through radiation, respectively. Introducing dimensionless quantities  $\eta = T/T_0$ ,  $\xi = r/r_0$ ,  $X = n_i/n_e$ ,  $\Lambda_{23}(\eta) = \Lambda(\eta T_0)/(10^{-23} \frac{\text{erg cm}^3}{\text{s}})$  and assuming that  $\gamma = 5/3$ , we obtain

$$\frac{d\eta}{d\xi} = -\frac{4}{3} \frac{\eta}{\xi} - \alpha \frac{\Lambda_{23}(\eta)}{\xi^2}, \quad (3)$$

\* In what follows, the temperature is in energy units and the opening angle is in radians. In this case, since the latter is small, we assume that  $\tan \Theta \approx \Theta$ .

$$\alpha = 10^{-23} \frac{\text{erg cm}^3}{\text{s}} \cdot \frac{2 n_{e0} r_0}{3 v T_0} \frac{X}{1+X}. \quad (4)$$

Substituting the input parameters typical of the jet in SS 433 and assuming that  $X \approx 0.91$ , we find

$$\alpha \approx 0.1272 \left( \frac{n_{e0}}{10^{14} \text{cm}^{-3}} \right) \left( \frac{r_0}{10^{11} \text{cm}} \right) \left( \frac{T_0}{20 \text{keV}} \right)^{-1} \left( \frac{v}{0.26c} \right)^{-1} \quad (5)$$

The limits of small and large  $\alpha$  correspond to adiabatic and quasi-cylindrical jets, respectively (see below and Section 4.3).

The emissivity  $\Lambda(T)$  in Eq. (2) is calculated in the model of a hot, optically thin plasma using the low-density limit (APEC, Smith et al. (2001)) by assuming solar elemental abundances (Lodders 2003)). A numerical solution of Eq. (3) with the parameter  $\alpha$  and the initial condition  $\eta_\alpha|_{\xi=1} = 1$  gives the temperature profile along the jet  $\eta_\alpha(\xi)$  or  $T(r) = T_0 \eta_\alpha(r/r_0)$ . Since  $\eta_\alpha(\xi)$  is a monotonic function of  $\xi$ , there exists an inverse function  $\xi_\alpha(\eta)$ . This allows the boundary of the computational domain  $\xi_{\max}$  to be determined, because thermal instabilities emerge in the jet at  $T_{\min} \sim 0.1 \text{ keV}$  (Kotani et al. 1996):  $\xi_{\max}(\alpha) = \xi_\alpha(T_{\min}/T_0)$ .

The number of free parameters can be reduced by fixing the total X-ray luminosity:

$$L_X = n_{e0}^2 r_0^3 \Theta^2 I(\alpha), \quad (6)$$

where

$$I(\alpha) = \pi X \int_1^{\xi_{\max}(\alpha)} \frac{\Lambda(T_0 \eta(\xi, \alpha))}{\xi^2} d\xi \quad (7)$$

The cooling at low  $\alpha$  is determined by adiabatic expansion, i.e.,  $\eta_\alpha(\xi) \approx \eta_0(\xi) = \xi^{-4/3}$  and  $\xi_{\max} = (T_{\min}/T_0)^{-3/4}$  do not depend on  $\alpha$ . Consequently,  $I(\alpha) \approx \text{const}$  and  $L_X = \text{const}$  implies

$$n_{e0}^2 r_0^3 \Theta^2 = \text{const}. \quad (8)$$

At large  $\alpha$ , in view of Eq. (3)  $\frac{\Lambda(T_0 \eta(\xi, \alpha))}{\xi^2} d\xi \propto \frac{d\eta}{\alpha}$ . Consequently,  $I(\alpha) \propto 1/\alpha$  and  $L_X = \text{const}$  implies

$$n_{e0} r_0^2 \Theta^2 = \text{const}, \quad (9)$$

which also corresponds to a constant mass loss rate in the jet  $\dot{M}_j = \text{const}$ .

## 3 RADIATIVE TRANSFER IN LINES

It is convenient to investigate the radiative transfer in a comoving frame of reference by getting rid of the constant longitudinal velocity component. The velocity field in such a frame is

$$v_{\parallel}(\vec{r}) = 0, \quad v_{\perp}(\vec{r}) = v_j * \tan(\theta), \quad v_j = 0.26c \quad (10)$$

In the introduced frame of reference, we will consider a line photon with energy  $E$  emitted on the jet axis in a direction  $\vec{\Omega}_0$  perpendicular to the jet axis. Since  $E, T \ll m_e c^2 = 511$  keV in the situation of interest to us, the optical depth to the jet edge for scattering by free electrons for such a photon is  $\tau_T(\xi) = n_e(\xi) \sigma_T r_0 \Theta \xi$ , where  $\sigma_T = 6.65 \cdot 10^{-25}$  cm<sup>2</sup> is the Thomson cross section. The calculation of the optical depth to the jet edge for resonant scattering on electron transitions in ions is slightly complicated by the velocity field (10). Therefore, we will initially assume that  $E = E_0$ , where  $E_0$  is the energy of the corresponding transition. Given the Doppler shift in the velocity field (10) and the fact that the direction  $\vec{\Omega}_0$  at each point is along the local velocity of the matter, we will then obtain

$$d\tau_{res}(\theta, \xi) = n_i(\xi) \sigma_0 \exp\left(-\left(\frac{v_\perp(\theta) E_0}{c \Delta E_D}\right)^2\right) r_0 \xi d\theta, \quad (11)$$

where  $\theta \in [0, \Theta]$  and, in view of the smallness of  $\Theta$ , along with  $\theta$ , we set  $\tan(\theta) \approx \theta$ . We also used the following standard notation:  $\sigma_0$  is the resonant scattering cross section at the line center and  $\Delta E_D$  is the line width due to the thermal motion of ions (for more details, see Section 4.1.2).

Denoting  $x = \frac{\beta E_0 \Theta}{\Delta E_D}$  ( $\beta = v_j/c = 0.26$ ),  $y = x \frac{\theta}{\Theta}$ ,  $\tau_{res}(\xi) = n_i(\xi) \sigma_0 r_0 \Theta \xi$  and integrating over  $y$ , we will obtain the total optical depth to the jet edge for resonant scattering for a photon emitted on the axis in the direction  $\vec{\Omega}_0$ :

$$\tau_{eff}(\xi) = \tau_{res}(\xi) \frac{\int_0^x e^{-y^2} dy}{x} = \tau_{res}(\xi) \frac{\Phi(x)}{x}, \quad (12)$$

where  $\Phi(x) = \frac{\sqrt{\pi}}{2} \text{erf}(x)$ ,  $\text{erf}(x)$  is the standard error function.

Let us now consider a photon also emitted on the jet axis in the direction  $\vec{\Omega}_0$  but with an initial energy shift  $\Delta E_0$  relative to the central value  $E_0$ , i.e.,  $E = E_0 + \Delta E_0$ . We see that for such a photon

$$d\tau_{res}(\theta, \xi) = n_i(\xi) \sigma_0 e^{-\left(\frac{\Delta E_0 - \beta E_0 \theta}{\Delta E_D}\right)^2} r_0 \xi d\theta, \quad (13)$$

and the total optical depth to the jet edge

$$\begin{aligned} \tau_{eff}(\xi, \Delta E_0) &= \tau_{res}(\xi) \frac{\int_0^{(1-\epsilon)x} e^{-y^2} dy}{x} = \\ &= \tau_{res}(\xi) \frac{\Phi((1-\epsilon)x) + \Phi(\epsilon x)}{x}, \end{aligned} \quad (14)$$

where  $\epsilon = \frac{\Delta E_0}{\beta \Theta E_0}$  is the initial shift parameter (in addition, we used the oddness of  $\text{erf}(x)$ ). Thus, the effective optical depth for resonant scattering can generally be written using the introduced notation as

$$\tau_{eff}(\xi, \Delta E_0) = \kappa_\epsilon(x) \tau_{res}(\xi). \quad (15)$$

The function  $\kappa_\epsilon(x) = \frac{\Phi((1-\epsilon)x) + \Phi(\epsilon x)}{x}$  (see Fig. 1) is such that:

- 1)  $\kappa_\epsilon(x) < 1$  for any  $x$  and  $\epsilon$ ;
- 2)  $\kappa_\epsilon(x)$  is symmetric relative to  $\epsilon = 0.5$ , i.e.  $\kappa_{0.5-\delta\epsilon}(x) = \kappa_{0.5+\delta\epsilon}(x)$  for any  $x$  and  $\delta\epsilon$ ;
- 3) for any  $x$  and  $\epsilon \neq 0.5$   $\kappa_\epsilon(x) < \kappa_{0.5}(x)$ ;
- 4) at large  $x$ ,  $\kappa_0(x) \sim 1/x$ ;

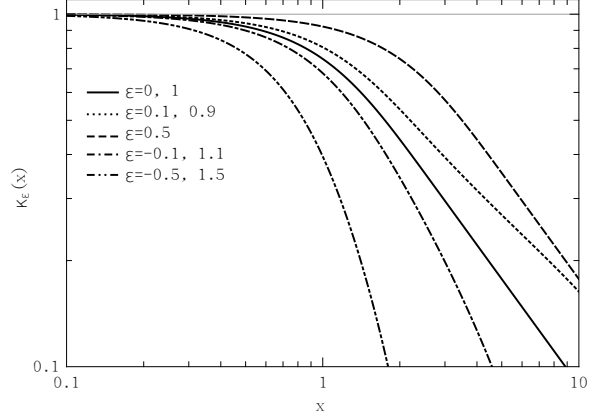


**Fig. 1.** General view of the function  $\kappa_\epsilon(x)$ , characterizing the resonant scattering efficiency as a function of  $x = \frac{\beta E_0 \Theta}{\Delta E_D}$  and the shift parameter  $\epsilon = \frac{\Delta E_0}{\beta \Theta E_0}$  according to Eq. (15)

Thus, it can be concluded that not the entire optical depth  $\tau_{res}$  but only some part of it  $\tau_{eff}$  is involved in the resonant scattering of the photon under consideration; the smaller the ratio of the thermal ion velocity to the bulk one specified by the velocity field (10), the smaller this part. In view of the asymptotics defined by property 4), this effect for a photon at the line center ( $\epsilon = 0$ ) is interpreted in such a way that the scattering at large  $x$  occurs only inside the cylinder at the boundary of which the bulk ion velocity is equal to the thermal one. This means that the estimate of  $\tau_{eff}(\xi, 0)$  remains valid not only for the photons emitted on the jet axis but also at any other point, except for the surface layer of thickness  $r_0 \Theta \xi / x$ . In addition, in view of properties (2) and (3), we can assume the profiles to be asymmetric relative to the central value due to the larger effective optical depth for high-energy photons ( $E > E_0, \epsilon > 0$ ) (as an illustration of these properties, see Fig. 2).

Let now the distribution of sources along the jet be defined by some function  $\phi(\xi)$ , i.e., the relative contribution of the layer  $d\xi$  to the total photon luminosity in the line is  $\phi(\xi) d\xi$ , and  $\int_1^{\xi_{max}} \phi(\xi) d\xi = 1$ . The weighted mean optical depths

$$\hat{\tau}_T = \int_1^{\xi_{max}} \tau_T(\xi) \phi(\xi) d\xi, \quad (16)$$

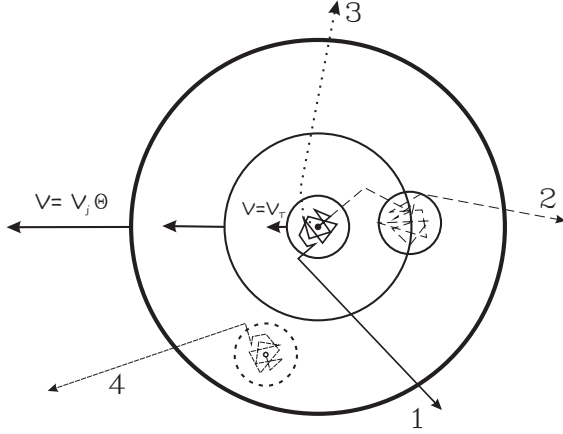


**Fig. 2.** Resonant scattering of photons in a layer perpendicular to the jet axis for  $x = \frac{\beta E_0 \Theta}{\Delta E_D} = \frac{V_T \Theta}{V_T} \sim 5$ . 1,2,3 – the pattern of the trajectory for photons emitted on the axis with  $E = E_0, E > E_0, E < E_0$  respectively; 4 – the pattern of the trajectory for a photon emitted not on the axis with  $E = E_0$

$$\hat{\tau}_{eff} = \int_1^{\xi_{max}} \tau_{eff}(\xi, \Delta E_0) \phi(\xi) d\xi \quad (17)$$

then characterize the influence of scattering on the integrated line emission.

To estimate the probability of the scattering by a free electron, we can use the critical optical depth  $\tau_{cr} = \frac{1}{2 \ln(\hat{\tau}_{eff}/\hat{\tau}_T)}$  following Pozdnyakov et al. (1983). At  $\hat{\tau}_T < \tau_{cr} < 1$ , the jet may be considered optically thin for scattering by electrons even for resonant photons. At  $\tau_{cr} < \hat{\tau}_T < 1$ , almost all of the photons will be scattered by the electron only once and, having left the line, form broad wings.

Undoubtedly, these estimates are qualitative in nature due to the dependence of  $\tau_{eff}$  on photon energy, the distribution of sources inside the layer  $d\xi$ , the velocity field (10), and the line overlap in the case of doublets and triplets. For a detailed analysis of the line formation, we have to resort to numerical simulations.

Since this work is aimed not at a theoretical study of the radiative transfer in lines but rather at its application for a specific physical object, we will restrict ourselves to the presented analysis, because the estimates obtained in its context can give a clear interpretation of the results obtained in our simulations (see the “Results” Section).

## 4 SPECTRUM SIMULATION

### 4.1 The Scheme of Computation

The approach used was developed by Pozdnyakov et al. (1983) and, subsequently, was successfully applied to investigate the radiative transfer in galaxy clusters (Sazonov et al. 2002; Zhuravleva et al. 2010).

#### 4.1.1 Emission

We will be interested in the radiation from a jet in the line corresponding to the transition from the upper level (UL) to the lower level (LL) in an  $n$ -fold ionized atom of element  $Z$  (for example, for the resonance  $K_\alpha$  lines of heliumlike atoms  $n = Z - 2$ , UL =  $1s2p(^1P_1)$  and LL =  $1s^2(^1S_0)$ ).

The dependences  $n_e(\vec{r})$  and  $T(\vec{r})$  found above allow the local ionization balance to be computed in the coronal approximation using AtomDB 2.0.1\*. As a result, in each  $\xi = \text{const}$  layer of thickness  $d\xi$  ( $d\xi \ll \Theta\xi$ ) we will obtain the density of ions of a given type  $n_i(\xi)$  and the plasma emissivity  $J(T)$  in the line of interest to us at temperature  $T = T_0\eta_\alpha(\xi)$ . The line photon production rate in such a layer is then defined as

$$dL(\xi) = \pi n_{e0}^2 r_0^3 \Theta^2 \frac{J(T_0\eta_\alpha(\xi))}{\xi^2} d\xi. \quad (18)$$

Thus,  $\phi(\xi) = \frac{1}{L_0} \frac{dL}{d\xi}$ , where the total luminosity

$$L_0 = \pi n_{e0}^2 r_0^3 \Theta^2 \int_1^{\xi_{max}(\alpha)} \frac{J(T_0\eta_\alpha(\xi))}{\xi^2} d\xi. \quad (19)$$

Similarly, for the continuum radiation

$$L_c(E) = \pi n_{e0}^2 r_0^3 \Theta^2 \int_1^{\xi_{max}(\alpha)} \frac{J_c(E, T_0\eta_\alpha(\xi))}{\xi^2} d\xi, \quad (20)$$

where  $J_c(E, T)$  is the plasma emissivity in the continuum per unit energy interval with center  $E$  at temperature  $T$  computed using the NoLine model of AtomDB 2.0.1 (kindly provided by Adam Foster<sup>†</sup>). The equivalent width of a line with a transition energy  $E_0$  is then defined as

$$EW = L_0 / L_c(E_0). \quad (21)$$

However, it is worth noting that the equivalent width defined in this way has no direct bearing on the observed quantities, because both jets contribute to the actual continuum, given the Doppler shift and relativistic collimation of the radiation. Nevertheless, assuming the jets to be identical, determining the observed equivalent width from the line equivalent width that we use for an arbitrary precession phase does not seem problematic.

#### 4.1.2 Scattering

The reciprocal of the mean free path (scattering coefficient) serves as a local characteristic defining the photon scattering probability:

$$\Sigma_x = n_x \sigma_x, \quad (22)$$

\*<http://atomdb.org/>;

<sup>†</sup>A description of the analogous model for APEC v1.3.1 can be found at <http://cxc.harvard.edu/twiki/bin/view/SnrE0102/NoLine>

where  $n_x$  is the number density of scattering centers and  $\sigma_x$  is the cross section for the corresponding scattering. For example, for scattering by electrons,  $\Sigma_e = n_e \sigma_T$ ,  $\sigma_T = 6.65 \cdot 10^{-25} \text{ cm}^2$  is the Thomson cross section. For resonant scattering by ions  $\Sigma_i = n_i \sigma_{res}$ ,  $\sigma_{res} = \sigma_0 \exp \left[ - \left( \frac{\Delta E}{\Delta E_D} \right)^2 \right]$ ,  $\sigma_0 = \frac{\sqrt{\pi} h r_e c f}{\Delta E_D}$ ,  $\Delta E_D = E_0 \left[ \frac{2T}{A m_p c^2} \right]^{1/2}$ ,  $\Delta E = E - E_0 \left( 1 + \frac{v}{c} \cos \psi \right)$ , where  $r_e$  is the classical electron radius,  $m_p$  is the proton mass,  $A$  is the atomic weight of the ion,  $E$  is the photon energy, and  $\psi$  is the angle between the photon direction and the local gas velocity determined by field (10). The energy  $E_0$  and oscillator strength  $f$  of the atomic transition can be found using AtomDB 2.0.1. It is worth noting that although the oscillator strength  $f$  is a basically positive quantity, in what follows (e.g., in Table 1), we take  $f = 0$  for transitions with  $f < 0.0001$  to simplify our calculations.

Whereas  $\Sigma_e$  depends only on the local electron density,  $\Sigma_i$  is a function of the local plasma characteristics ( $n_e$  and  $T$ ), the photon energy and direction.

We performed detailed Monte Carlo simulations of the emergent radiation spectrum in lines. We used a scheme with a statistical “weighting” of photon packets, along with the method of a constant total cross section (Sobol’ 1973). The idea of this method is to introduce, along with the real types of scattering, some fictitious scattering, such that

$$\Sigma_{fict} = \Sigma_0 - (\Sigma_e + \Sigma_i), \quad (23)$$

where the constant  $\Sigma_0$  is greater than or equal to the maximum possible  $\Sigma_{real} = \Sigma_e + \Sigma_i$ . As a result, the inhomogeneous (in the sense of local scattering characteristics) medium is replaced by a homogeneous one with a small mean free path  $\lambda = \Sigma_0^{-1}$ . In each scattering, the realization probability of a particular type is defined as  $p_x = \Sigma_x / \Sigma_0$ . In the case of fictitious scattering, both direction and energy of the photon package remain unchanged. The resonant scattering by ions is represented as a combination of the dipole and isotropic components. The weight of the dipole component  $w_d$  is determined by the total angular momentum of the lower level  $j_{LL}$  and by the difference  $\Delta j = j_{UL} - j_{LL}$  (Hamilton 1947).

The described scheme can be extended to the simulation of unresolvable multiplets (the photons fall into the total spectrum “weighted” proportionally to the parent line intensity, while the scattering on each multiplet component is considered as a separate type of scattering). The addition of a broad continuum component and the calculation of its scattering are also possible.

#### 4.2 The Set of Lines

To form the set of simulated lines, the best resolution Chandra HETGS spectra (Marshall et al. 2002; Namiki et al. 2003; Lopez et al. 2006) should be used. The brightest observed lines subject to strong scattering effects correspond to the  $K_\alpha$  transitions in helium-like ions and to

the  $Ly_\alpha$  transitions in hydrogen-like ions with significant oscillator strengths whose parameters are listed in Table 1. In this case, the  $K_\alpha$  transitions in helium-like ions have a triplet structure (the resonance (w), intercombination (x + y), and forbidden (z) lines). Bearing in mind the importance of these lines for diagnosing the jet plasma parameters, we performed detailed simulations of the components by taking into account the possible interaction via the optical depths and the influence of collisions on the upper level population of the forbidden and intercombination transitions at  $n_e$  greater than some  $n_{e,crit}$  (Porquet et al. 2010). In addition, in some cases, the influence of satellites on the intensity ratio of these lines should be taken into account (see the “Results” Section).

#### 4.3 Input parameters

There is a considerable uncertainty in the physical parameters of the jets in SS 433. Based on Chandra HETGS observations at the phase of the greatest disk opening toward the observer, Marshall et al. (2002) obtained  $r_0 \simeq 2 \times 10^{10} \text{ cm}$ ,  $n_{e0} \simeq 2 \times 10^{15} \text{ cm}^{-3}$ ,  $T_0 \simeq 13 \text{ keV}$ , and  $\Theta \simeq 0.01 \text{ rad}$  for the approaching jet. Analysis of the XMM-Newton X-ray spectra also at the phase of the greatest opening (Medvedev, Fabrika 2010) gives  $r_0 \simeq 2 \times 10^{11} \text{ cm}$  and  $T_0 \simeq 17 \text{ keV}$  for the approaching jet. In contrast, studies based on the eclipse of the jets by the optical companion yield  $r_0 \sim 1 \times 10^{12} \text{ cm}$  and  $T_0 \sim 30 \text{ keV}$  (Filippova et al. 2006).

Therefore, two classes of models satisfying condition (6) for the conservation of total X-ray luminosity were formed – for the pair of jets  $L_x \sim 10^{36} \text{ erg/s}$  (Medvedev, Fabrika 2010) in the range from 0.1 to 50 keV either in form (8) (the class of quasi-adiabatic models) or in form (9) (the class of quasi-cylindrical models), depending on the parameter  $\alpha$ . Since the available observations can reliably set only an upper limit on the opening angle (see Section 6), we allowed  $\Theta$  to change in a very wide range. For this reason, precisely  $\Theta$  served as a class-forming parameter (in the sense of discrimination by  $\alpha$ ). As a result, the simulations were performed on a wide grid of input parameters given in Table 2 and encompassing the most probable values. The quasiadiabatic models correspond to  $\Theta = 0.01 \text{ rad}$  and  $\Theta = 0.02 \text{ rad}$ , while the quasi-cylindrical ones correspond to  $\Theta = 0.003 \text{ rad}$  and  $\Theta = 0.0001 \text{ rad}$ . We considered  $T_0 = 20 \text{ keV}$  and  $T_0 = 30 \text{ keV}$  as possible plasma temperatures at the jet base. The abundances of heavy elements were assumed to be solar (Lodders 2003).

It is worth noting that whereas in the case of quasi-adiabatic models  $r_0$  roughly coincides with the distance from the jet base to the compact object, in the case of quasi-cylindrical models  $r_0$  has the meaning of only a geometrical parameter of the flow. Therefore, using the combination  $r_0 \Theta$ , which means the transverse size of the jet near its base, appears more preferable for the description of a particular model in the general case.

**Table 1.** The set of simulated lines. The asterisk (\*) marks the lines for which we do not present our simulation results but which are used in constructing the total broadband spectrum (see the Conclusions). The expression  $f = 0$  should be understood in the sense that  $f < 0.0001$  (see also the text)

Spectroscopic symbol	Transition	$E_0$ , keV	f	$w_d$
Fe XXV	$K_\beta : 1s^2 - 1s3p (^1P_1)$	7.881	0.14	1
Ni XXVII	$K_\alpha : 1s^2 - 1s2p (^1P_1)(w)$	7.806	0.72	1
Ni XXVII	$K_\alpha : 1s^2 - 1s2p (^3P_2)(x)$	7.799	0	-
Ni XXVII	$K_\alpha : 1s^2 - 1s2p (^3P_1)(y)$	7.766	0.07	1
Ni XXVII	$K_\alpha : 1s^2 - 1s2p (^3S_1)(z)$	7.744	0	-
Fe XXVI	$Ly_\alpha : 1s - 2p (^1P_{3/2})$	6.973	0.27	0.5
Fe XXVI	$Ly_\alpha : 1s - 2p (^1P_{1/2})$	6.952	0.14	0
Fe XXV	$K_\alpha : 1s^2 - 1s2p (^1P_1)(w)$	6.700	0.78	1
Fe XXV	$K_\alpha : 1s^2 - 1s2p (^3P_2)(x)$	6.682	0	-
Fe XXV	$K_\alpha : 1s^2 - 1s2p (^3P_1)(y)$	6.667	0.07	1
Fe XXV	$K_\alpha : 1s^2 - 1s2p (^3S_1)(z)$	6.636	0	-
Ca XIX *	$K_\alpha : 1s^2 - 1s2p (^1P_1)$	3.902	0.77	1
Ar XVII *	$K_\alpha : 1s^2 - 1s2p (^1P_1)$	3.133	0.77	1
S XVI *	$Ly_\alpha : 1s - 2p (^1P_{3/2})$	2.623	0.27	0.5
S XVI *	$Ly_\alpha : 1s - 2p (^1P_{1/2})$	2.620	0.14	0
S XV	$K_\alpha : 1s^2 - 1s2p (^1P_1)(w)$	2.461	0.76	1
S XV	$K_\alpha : 1s^2 - 1s2p (^3P_2)(x)$	2.449	0	-
S XV	$K_\alpha : 1s^2 - 1s2p (^3P_1)(y)$	2.447	0.07	1
S XV	$K_\alpha : 1s^2 - 1s2p (^3S_1)(z)$	2.430	0	-
Si XIV *	$Ly_\alpha : 1s - 2p (^1P_{3/2})$	2.006	0.27	0.5
Si XIV *	$Ly_\alpha : 1s - 2p (^1P_{1/2})$	2.004	0.14	0
Si XIII	$K_\alpha : 1s^2 - 1s2p (^1P_1)(w)$	1.865	0.75	1
Si XIII	$K_\alpha : 1s^2 - 1s2p (^3P_2)(x)$	1.855	0	-
Si XIII	$K_\alpha : 1s^2 - 1s2p (^3P_1)(y)$	1.854	0.07	1
Si XIII	$K_\alpha : 1s^2 - 1s2p (^3S_1)(z)$	1.839	0	-

To illustrate the physical picture that emerges when considering the constructed grid of parameters through the prism of the jet model from Section 2, it is convenient to use the profiles of temperature  $T(\xi)$  (Fig. 3), optical depth  $\tau_x(\xi) = \Theta \xi r_0 \Sigma_x$ , and flux  $\phi_i(\xi)$  (Fig. 4) in lines.

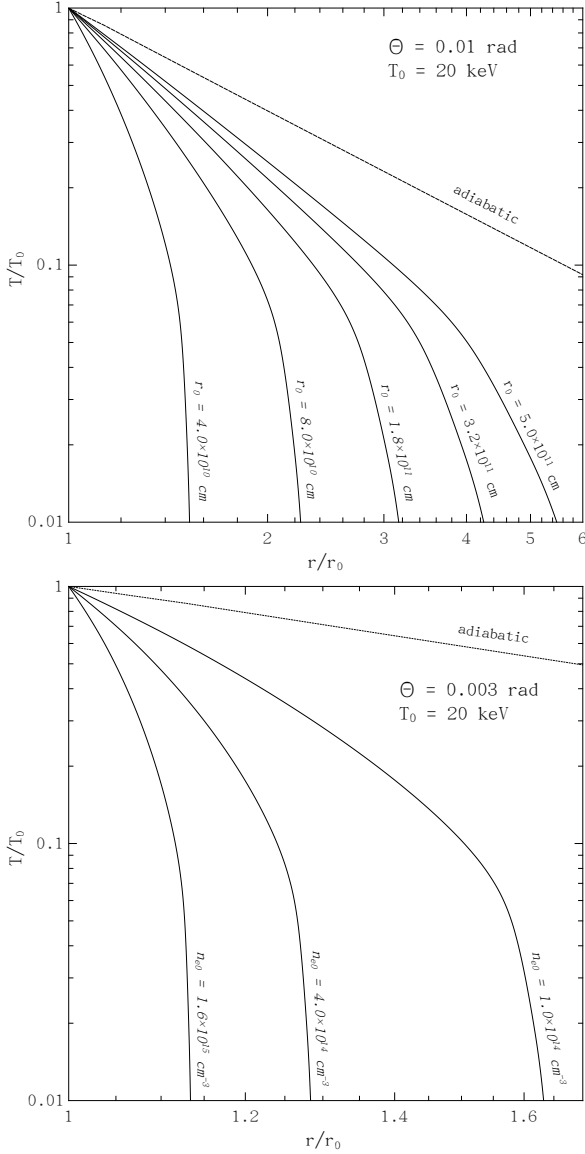


**Fig. 3.** Temperature profiles along the jet for various input parameters from Table 2

## 5 RESULTS

### 5.1 Lines

To save space, we present the results of our computations only for the most important (in our view) lines of the approaching jet with  $T_0 = 20$  keV at the phase of the greatest disk opening that corresponds to an angle between the jet axis and the observer's direction  $\chi \approx 65^\circ$ , i.e., a redshift  $z_b = -0.078$  ( $z = \gamma(1 - \beta \cos \chi) - 1$ ,  $\gamma = 1/\sqrt{1 - \beta^2}$ ,  $\beta =$

$v_j/c = 0.26$ ). The results for the remaining (marked by \* in Table 1) lines are used only in constructing the total broadband spectrum (see the Conclusions). Analysis of our computations for other precession phases and  $T_0 = 30$  keV showed that the general conclusions (see the Conclusions) remain valid here as well, while most of the changes are equivalent to some shift on the constructed grid of parameters in the sense of scattered line characteristics.

The main quantitative characteristic reflecting the influence of scattering effects on the observed spectrum is the fraction of the photons  $\zeta$  that left the line as a result of their scattering by a free electron and that fell into the broad wings. Together with the temperature  $T_e$  providing the best agreement between the shape of the broad wings and the single Compton scattering kernel (Sazonov, Sunyaev 2000), the parameter  $\zeta$  allows the contribution of scattered radiation to the continuum to be completely described (for more details, see Section 5.2). Since it is probably impossible to find such a complete and universal way of describing the shape of the scattered line itself, one has to content oneself with standard approximations when analyzing the derived profiles. This approach is justified from the viewpoint of observational characteristics of existing spectrometers (Chandra HETGS), which do not allow the fine structure of the line profiles to be investigated in most cases. However, it is clearly insufficient from the viewpoint of new-generation X-ray observatories (primarily Astro-H). For this reason, the set of parameters, except for the line attenuation coefficient equal to  $(1 - \zeta)$ , is determined by the specific simplifying model that is most appropriate for the line in the resolution of a particular instrument (Chandra HETGS (to be more precise, HEG–High Energy Gratings) or Astro-H SXS).

To analyze the spectra in the Chandra HEG resolution, we used a model response function in the form of a Gaussian with  $FWHM_{Ch}(E_z) = 29.9 \text{ eV} \left(\frac{E_z}{6.4 \text{ keV}}\right)^2$  (in accordance with the Chandra Gratings Fact Sheet \*), where  $E_z = E_z/(1 + z)$ . For Astro-H SXS, we used a Gaussian with  $FWHM_{AH}(E_z) = 5 \text{ eV} = \text{const}$  (in accordance with the Astro-H Quick Reference †).

Since all lines exhibit very similar patterns in various regimes of radiative transfer, we will restrict ourselves to a detailed description and interpretation of the results only for the  $K_\alpha$  triplet of helium-like iron, providing the scattering features in a specific line, where necessary.

#### 5.1.1 Fe XXV $K_\alpha$

The helium-like iron triplet is brightest among the observed lines (Table 2). Nonetheless, only the components corresponding to the allowed transitions with  $f > 0$  (see Table 1) can have a significant intrinsic optical depth for

\*[https://icxc.harvard.edu/rws/peer\\_review/proc\\_docs/Fact\\_Sheet\\_gratings.pdf](https://icxc.harvard.edu/rws/peer_review/proc_docs/Fact_Sheet_gratings.pdf)

†<http://astro-h.isas.jaxa.jp/doc/ahqr.pdf>

resonant scattering. At the same time, the line broadening due to the transverse velocity component at  $\Theta \sim 0.01$  rad is enough to overlap the resonance and intercombination lines. This makes the interaction between the components via the optical depths possible and, consequently, indicates that all components should be taken into account simultaneously when the local characteristics of the scattering medium are calculated.

The computation performed with the Cloudy code (version 08.00 described by Ferland et al. (1998)) in the temperature range of interest to us showed that for helium-like iron  $n_{e,crit} \sim 10^{17} \text{ cm}^{-3}$  is the density at which the collisional excitations from  $^3S_1$  (the upper level of the forbidden component) to  $^3P_{0,1,2}$  (the upper levels of the intercombination components) begin to dominate over the radiative transition from  $^3S_1$  to the ground level. Thus, on the specified grid of parameters  $n_0 \ll n_{e,crit}$ , i.e., the intensity redistribution of the forbidden and intercombination lines for iron may be neglected. Note that this conclusion is also valid for the nickel triplet, because  $n_{e,crit} = \frac{A_{fg}}{C_{fi}} \propto Z^{13}$  (Mewe, Schrijver 1978a), where  $A_{fg}$  is the rate of radiative transitions to the ground level and  $C_{fi}$  is the rate of collisional excitations to the upper levels of the intercombination lines.

The results of our analysis of the simulated spectra in the Chandra HEG resolution are presented in Table 3. Since  $FWHM_{Ch}$  at  $E_z \simeq 7 \text{ keV}$  exceeds the expected line  $FWHM_0 = \sqrt{3}\gamma\beta\Theta \sin\chi E_z$  (Marshall et al. 2002) ( $\chi \approx 65^\circ$  is the angle between the jet axis and the observer's direction) for  $\Theta \simeq 0.01$  rad (see Fig. 5), we fitted the spectrum convolved with the model response function by **three** Gaussians of the same FWHM but with decoupled centroids ( $E_f, E_i, E_r$  in the rest frame of the jet) and amplitudes  $f, i, r$  (without scattering  $(f/r)_0 = 0.28$ ,  $(i/r)_0 = 0.27$  (see Table 3). In what follows, the tables of results give the line width  $W$  minus the instrumental broadening (i.e.,  $W = \sqrt{FWHM^2 - FWHM_{Ch}^2}$  and  $W = \sqrt{FWHM^2 - FWHM_{AH}^2}$  in the cases of analysis in the Chandra HEG and Astro-H resolutions, respectively).

The attenuation coefficient  $(1 - \zeta)$  was calculated for the triplet as a single line with a centroid  $E_c$  (the first moment of the photon number distribution in energy), i.e., its boundaries were determined with respect to the common broad wings (see Table 3).

Since the spectra convolved with the Astro-H model response function cannot be described in such a way, we provide only some of the derived line profiles (Fig. 5), which illustrate the characteristic features of a particular scattering regime. The energy  $E$  in the observer's frame of reference is along the horizontal axis; the fraction of all line photons with energies in the range from  $E - \Delta E/2$  to  $E + \Delta E/2$ , where  $\Delta E \ll FWHM$  is the spectral bin size, is along the vertical axis.

As has been noted above, the triplet components at  $\Theta \geq$

0.01 rad actively interact via the optical depths, what distorts noticeably the line shape. For  $\Theta = 0.02$  rad the transverse optical depth of the jet for Thomson scattering  $\hat{\tau}_T$  turns out to be less than a critical value  $\tau_{cr} \approx 0.19$  (see the "Radiative Transfer in Lines" Section) for the resonance line photons at  $r_0 > 4 \times 10^{10} \text{ cm}$ ; therefore, the scatterings by electrons cause all triplet lines to be suppressed to approximately the same degree. The fraction of the photons that left the line  $\zeta$  reaches 30% at  $r_0 = 4 \times 10^{10} \text{ cm}$ . Note that for  $\Theta = 0.02$  rad the quantities  $E_f, E_i, E_r$  and  $f, i, r$  found in our analysis lose their physical linkage to the forbidden, intercombination, and resonance lines, respectively, and basically have only a descriptive significance.

For  $\Theta = 0.01$  rad the interaction between the components still remains significant, but the "extension" of the optical depth to the low-energy region for the resonance line photons becomes its main manifestation. In this case,  $\hat{\tau}_T$  turns out to be greater than  $\tau_{cr} \approx 0.15$  for the resonance photons already at  $r_0 = 8 \times 10^{10} \text{ cm}$ . This enhances the escape into the wings  $\zeta$  and increases the relative intensities of the forbidden (f/r) and intercombination (i/r) lines (see Table 3). Thus, the fraction of the photons that left the line turns out to be significant, but, nevertheless,  $\zeta \leq 40\%$  for the entire triplet due to the photons emitted inside the surface layer (see the "Radiative Transfer in Lines" Section) and the contribution from the forbidden and intercombination components. Another effect is the increase in line width  $W$  as a result of multiple scatterings.

For  $\Theta = 0.003$  rad the interaction between the components no longer plays a significant role, while  $\hat{\tau}_T$  turns out to be greater than  $\tau_{cr} \approx 0.11$  for the resonance photons already at  $n_{e0} > 1 \times 10^{14} \text{ cm}^{-3}$ . Therefore, the resonance line is suppressed noticeably in comparison with the forbidden and intercombination lines. The existence of a transverse velocity gradient has an effect on the strong asymmetry of the resonance line profile, in agreement with the predictions made in the "Radiative Transfer in Lines" Section. The additional broadening also becomes more pronounced.

In the cylindrical case of  $\Theta = 0.0001$  rad, the transverse velocity gradient is negligible and almost all of the resonance line photons produced deep in the jet are ultimately scattered by an electron and fall into the broad line wings. Thus, in a sense, a pure case is realized, i.e., only the photons emitted in the jet surface layer remain at the resonance line center. As a result, the entire triplet noticeably loses in intensity, while the relative contribution of the forbidden and intercombination lines increases. In this case, the width of the lines exceeds that of the unscattered lines at  $\Theta = 0.003$  rad and is less than that of the scattered lines at  $\Theta = 0.01$  rad by only a factor of 1.5. Given the additional possibilities for broadening (see Section 5.3), this indicates that  $\Theta$  is difficult to measure accurately based on Chandra HETGS observations of the helium-like iron  $K_\alpha$  triplet. In turn, Astro-H is ideally suited for studying the fine structure of this line and diagnosing the jet parameters from it.



**Table 2.** The grid of input parameters and the corresponding values of  $\alpha$  at  $T_0 = 20$  keV as well as the luminosities ( $L_n = L/10^n$ ) and equivalent widths (without scattering) of the lines from Table 1 for which detailed simulation results are presented (see the “Results” Section). The use of the quasi-cylindrical calibration (9) when passing from  $r_0 = 8 \times 10^{10}$  cm to  $r_0 = 4 \times 10^{10}$  cm for  $\Theta = 0.01$  and  $\Theta = 0.02$  rad is marked (\*), because  $\alpha \sim 1$  in this case

$r_0\Theta$ 10 <sup>9</sup> cm	$n_{e0}$ 10 <sup>14</sup> cm <sup>-3</sup>	$\alpha$	Fe XXV K $_{\alpha}$		Fe XXVI Ly $_{\alpha}$		Ni XXVII K $_{\alpha}$		Fe XXV K $_{\beta}$		S XV K $_{\alpha}$		Si XIII K $_{\alpha}$	
			L <sub>33</sub> , erg/s	EW eV	L <sub>33</sub> erg/s	EW eV	L <sub>32</sub> erg/s	EW eV	L <sub>32</sub> erg/s	EW eV	L <sub>33</sub> erg/s	EW eV	L <sub>33</sub> erg/s	EW eV
Quasi-adiabatic models														
$\Theta = 0.02$ rad														
10.0	0.16	0.10	8.7	227	5.00	164	5.59	21	9.11	34	0.99	13.3	1.48	15.4
6.4	0.31	0.13	8.4	230	4.73	163	5.34	21	8.74	35	0.91	13.7	1.44	15.8
3.6	0.75	0.17	8.4	234	4.63	163	5.34	22	8.7	35	0.85	14.2	1.44	15.9
1.6	2.5	0.25	7.4	239	4.00	162	4.66	22	7.7	36	0.65	14.3	1.23	15.4
0.8	10.0 <sup>†</sup>	0.51	11.1	242	5.88	162	6.91	22	11.47	37	0.98	13.6	1.61	13.7
$\Theta = 0.01$ rad														
5.0	0.32	0.20	7.8	238	4.29	163	4.96	22	8.17	36	1.04	14.3	1.34	15.7
3.2	0.62	0.25	7.3	239	3.94	162	4.58	22	7.57	36	1.03	14.3	1.21	15.4
1.8	1.5	0.34	6.9	241	3.68	162	4.3	22	7.13	36	1.05	14.1	1.09	14.8
0.8	5.0	0.51	5.6	242	2.95	162	3.46	22	5.73	37	0.93	13.6	0.80	13.7
0.4	20.0 <sup>†</sup>	1.02	7.0	240	3.76	162	4.38	22	7.24	36	1.30	12.4	0.89	12.1
Quasi-cylindrical models														
$\Theta = 0.003$ rad														
2.0	1.0	8.69	9.0	241	4.84	162	5.62	22	9.3	36	0.99	12.6	1.17	12.4
1.0	4.0	17.38	10.1	237	5.54	163	6.4	22	10.34	36	1.04	11.9	1.22	11.3
0.5	16.0	34.77	10.8	234	6.03	163	6.89	22	11.31	35	1.08	11.4	1.24	10.8
$\Theta = 0.0001$ rad														
2.0	1.0	26.07	11.5	231	6.59	163	7.46	21	12.22	35	1.12	10.9	1.28	10.3
1.0	4.0	52.15	11.5	231	6.52	163	7.35	21	12.03	35	1.10	10.8	1.26	10.3
0.5	16.0	104.30	11.5	231	6.52	163	7.37	21	12.06	35	1.10	10.8	1.26	10.4

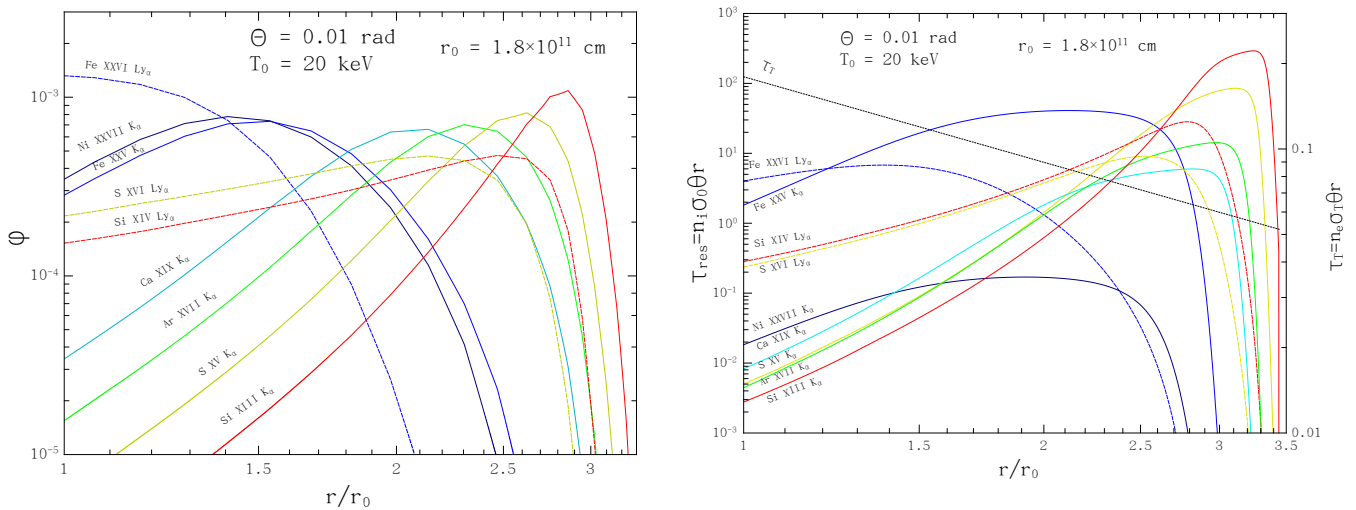


**Fig. 4.** **Left** – Contribution from various jet regions to the total luminosity  $\phi(\xi) = \frac{1}{L_0} \frac{dL}{d\xi}$  in some of the lines from Table 1. **Right** – Profiles of the transverse optical depth of the jet for scattering by electrons and resonant scattering in some of the lines from Table 1.

**Table 3.** Analysis of the simulation results for the FeXXV  $K_\alpha$  triplet in the Chandra resolution for the approaching jet with  $T_0 = 20$  keV at a phase corresponding to  $z_b = -0.078$ . The widths of the unscattered lines are  $W_0 = 37.8$  eV at  $\Theta = 0.02$  rad,  $W_0 = 24.0$  eV at  $\Theta = 0.01$  rad,  $W_0 = 13.3$  eV at  $\Theta = 0.003$  rad, and  $W_0 = 11.9$  eV at  $\Theta = 0.0001$  rad

	$1-\zeta$	$E_c$ , keV	$W$ , eV	$f/r$	$i/r$	$E_f$ , keV	$E_i$ , keV	$E_r$ , keV
$r_0, 10^{11}$ cm $\Theta=0.02$ rad								
5.0	0.95	6.6835	38.2	0.315	0.630	6.6336	6.6736	6.7048
3.2	0.93	6.6835	38.2	0.310	0.612	6.6340	6.6727	6.7047
1.8	0.91	6.6833	38.3	0.303	0.600	6.6339	6.6716	6.7047
0.8	0.85	6.6833	38.1	0.287	0.587	6.6340	6.6695	6.7051
0.4	0.69	6.6838	37.0	0.252	0.563	6.6340	6.6661	6.7063
$r_0, 10^{11}$ cm $\Theta=0.01$ rad								
5.0	0.95	6.6876	25.2	0.290	0.276	6.6371	6.6721	6.6992
3.2	0.93	6.6852	25.5	0.293	0.274	6.6374	6.6721	6.6990
1.8	0.88	6.6831	25.9	0.298	0.274	6.6378	6.6721	6.6989
0.8	0.81	6.6829	26.1	0.307	0.275	6.6384	6.6721	6.6989
0.4	0.62	6.6826	26.2	0.338	0.281	6.6397	6.6730	6.6995
$n_{e0}, 10^{14}$ cm $^{-3}$ $\Theta=0.003$ rad								
1	0.86	6.6824	15.9	0.311	0.300	6.6372	6.6731	6.6985
4	0.71	6.6813	16.8	0.350	0.333	6.6376	6.6741	6.6984
16	0.51	6.6800	17.3	0.438	0.408	6.6381	6.6758	6.6990
$n_{e0}, 10^{14}$ cm $^{-3}$ $\Theta=0.0001$ rad								
1	0.80	6.6820	14.7	0.338	0.334	6.6370	6.6733	6.6994
4	0.64	6.6803	15.4	0.406	0.392	6.6372	6.6745	6.6996
16	0.45	6.6781	15.6	0.515	0.486	6.6373	6.6758	6.6999

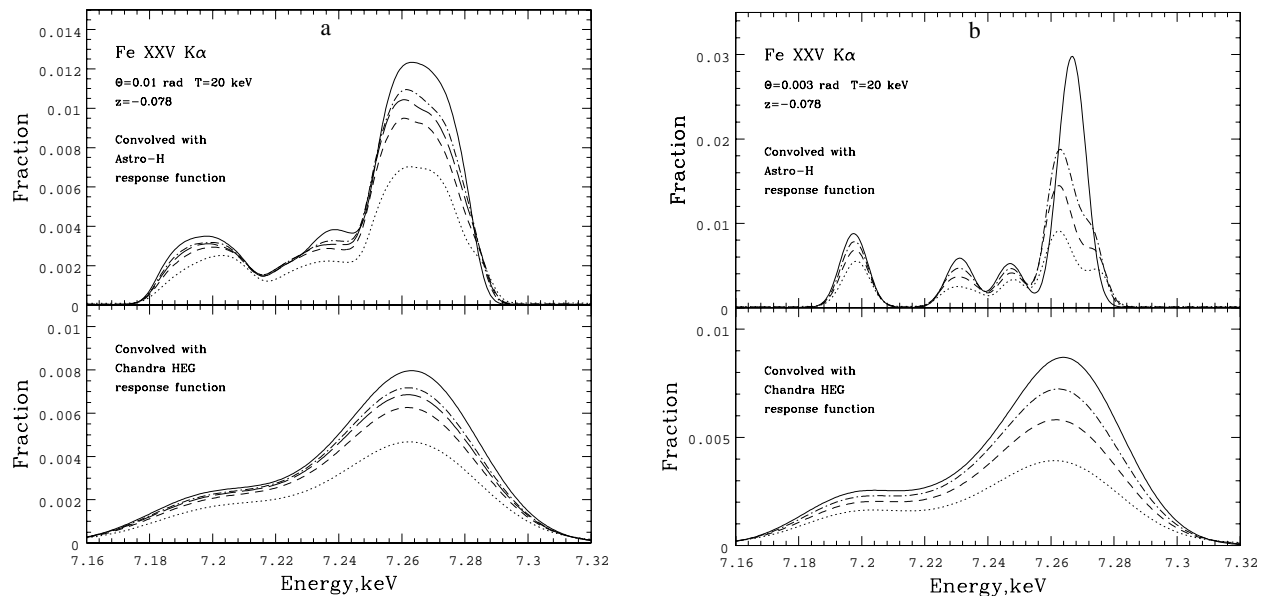


**Fig. 5.** Results of our simulations for the FeXXV  $K_\alpha$  triplet for the approaching jet with  $T_0 = 20$  keV at a phase corresponding to  $z_b = -0.078$ . (a)  $\Theta = 0.01$ ; the upper panel shows the spectrum convolved with the Astro-H model response function; the lower panel shows the spectrum convolved with the Chandra HEG model response function; the dotted curve for  $r_0 = 4 \times 10^{10}$  cm, the curve with short dashes for  $r_0 = 8 \times 10^{10}$  cm, the curve with long dashes for  $r_0 = 1.8 \times 10^{11}$  cm, the dash-dotted curve for  $r_0 = 3.2 \times 10^{11}$  cm, and the solid curve indicates the unscattered line profile (the same for all  $r_0$ ). (b)  $\Theta = 0.003$  rad; the upper panel shows the spectrum convolved with the Astro-H model response function; the lower panel shows the spectrum convolved with the Chandra HEG model response function; the dotted curve for  $n_{e0} = 1.6 \times 10^{15}$  cm $^{-3}$ , the curve with short dashes for  $n_{e0} = 4 \times 10^{14}$  cm $^{-3}$ , the dash-dotted curve for  $n_{e0} = 1.0 \times 10^{14}$  cm $^{-3}$ , and the solid curve indicates the unscattered line profile (the same for all  $n_{e0}$ )

### 5.1.2 Fe XXVI $Ly_\alpha$

Since the FeXXVI  $Ly_\alpha$  doublet corresponds to the transitions in hydrogenlike iron, both emissivity and optical depth of the jet plasma in these lines have a peak at slightly higher temperatures than those in the helium-like iron  $K_\alpha$  triplet lines (see Fig. 4). This allows the Fe XXVI  $Ly_\alpha$ / Fe XXV  $K_\alpha$  ratio to be used to diagnose the temperature of the hottest parts of the jet (Kotani et al. 1996).

In this case, the oscillator strength  $f$  for the  $Ly_\alpha$  transitions is considerably (approximately by a factor of 3 for the  $1s-2p$  ( $^1P_{3/2}$ ) transition and approximately by a factor of 6 for the  $1s-2p$  ( $^1P_{1/2}$ ) transition; see Table 1) smaller than that for the resonance component of the  $K_\alpha$  triplet, whence, at first glance, the doublet lines can be assumed to be less subjected to the scattering effects inside the jet. However, the Doppler energy shift due to the transverse jet plasma velocity component at  $\Theta \sim 0.01$  rad allows the photons of the higher-energy doublet component to be efficiently scattered on the transition corresponding to the low-energy component. As a result, the scattered line for  $\Theta = 0.01$  rad has a completely different profile compared to the initial one (see Fig. 6); for its description in the Astro-H resolution, we used a model consisting of two Gaussians of the same FWHM with amplitudes A1 and A2 and centroids shifted by  $\delta z_1$  and  $\delta z_2$  relative to the initial positions for the low- and high-energy components, respectively (Table 5).

When analyzing the spectra in the Chandra HEG resolution, we used a model of a single Gaussian with FWHM with a centroid corresponding to the weighted mean energy of the unscattered doublet (Table 4). The attenuation coefficient  $(1 - \zeta)$  is given for the doublet as a single line. Typical scattered line profiles are shown in Fig. 6.

Although for  $\Theta = 0.02$  rad and  $\Theta = 0.01$  rad  $\hat{\tau}_T$  is less than  $\tau_{cr}$  for the photons of the high-energy component at all  $r_0$ , except for  $r_0 = 4 \times 10^{10}$  cm, the total doublet intensity decreases considerably. This is probably a result of the above-mentioned extension of the optical depth to the red region for the photons of the high-energy component. This effect is clearly illustrated by the results of our analysis of the scattered doublet profiles in the Astro-H resolution (Table 5). The increase of  $A_1/A_2$  with decreasing  $r_0$  allows the “flattening” of the doublet profile to be judged, while the centroid shifts  $\delta z_1$  and  $\delta z_2$  point to the absence of a physical linkage of the fitting Gaussians to the doublet components. In addition, the effective line broadening turns out to be very significant (Table 4).

For  $\Theta = 0.003$  rad and  $\Theta = 0.0001$  rad, in the absence of any interaction between the components, the scattering pattern is completely identical to that described in detail for the  $K_\alpha$  triplet. In this case, the scattered line width  $W$  from our analysis in the Chandra HEG resolution turns out to be approximately equal to the unscattered line width  $W_0$  for  $\Theta = 0.01$  rad.

Thus, owing to the interaction between the components,

the influence of scattering effects turns out to be significant (primarily on the line profiles) even at large  $\Theta$  almost on the entire grid of parameters. This makes the fine structure of the  $Ly_\alpha$  doublet profile a very sensitive tool for diagnosing the hottest parts of the jet, in particular, based on Astro-H observations.

**Table 5.** Analysis of the simulation results for the FeXXVI  $Ly_\alpha$  doublet in the Astro-H resolution for the approaching jet with  $T_0 = 20$  keV corresponding to  $z_b = -0.078$ .

$\Theta = 0.01$ rad				
$r_0, 10^{11}$ cm	A1/A2	W, eV	$\delta z_1, 10^{-4}$	$\delta z_2, 10^{-4}$
5.0	0.66	26.18	1.46	-1.69
3.2	0.69	25.73	1.34	-2.17
1.8	0.73	25.57	1.59	-2.66
0.8	0.78	24.96	2.20	-3.52
0.4	0.80	24.78	1.48	-5.20

### 5.1.3 Ni XXVII $K_\alpha$ + Fe XXV $K_\beta$

The currently available observations near the nickel  $K_\alpha$  triplet point to an excess of radiation compared to that expected from the FeXXV (6.7 keV) line intensity within the standard model with solar elemental abundances (Table. 2). This is interpreted in terms of a nickel overabundance in the jet plasma (Brinkmann et al. (2005), Medvedev, Fabrika (2010)). Since present-day instruments do not allow NiXXVII  $K_\alpha$  and FeXXV  $K_\beta$  to be reliably resolved, we performed joint simulations of these lines, although a noticeable overlap takes place only for  $\Theta = 0.02$  rad (see Fig. 7).

We do not provide the results of our analysis of the simulated spectra in the Chandra HEG resolution due to the low sensitivity of this instrument near  $E_z \simeq 8.5$  keV.

When analyzing the spectra in the Astro-H resolution, we used a model consisting of five Gaussians of the same FWHM with decoupled amplitudes but fixed centroids. The attenuation coefficients  $(1 - \zeta)$  are determined separately for the nickel triplet and  $K_\beta$  of helium-like iron (see Table 6).

Whereas  $\hat{\tau}_T$  is much less than  $\tau_{cr}$  for the photons of the nickel resonance line on the entire grid of quasiadiabatic model parameters,  $\tau_{cr}$  is not so large for the photons of the iron  $K_\beta$  line and even turns out to be less than  $\hat{\tau}_T$  at  $\Theta = 0.01$  rad and  $r_0 = 4 \times 10^{10}$  cm. In particular, this is reflected in different dependences of  $\zeta$  on  $r_0$  (see Table refnifeah). As a result, the F(Ni)/F(Fe) ratio slightly changes, but this change takes place only at  $r_0 = 4 \times 10^{10}$  cm and does not exceed 10% in magnitude. Thus, the main effect is a general decrease in intensity due to Thomson scattering almost on the entire grid of quasi-adiabatic model parameters.

For the quasi-cylindrical models, the overall pattern of radiative transfer is very similar to the case of the FeXXV

**Table 4.** Analysis of the simulation results for the FeXXVI  $L\gamma_\alpha$  doublet in the Chandra resolution for the approaching jet with  $T_0 = 20$  keV corresponding to  $z_b = -0.078$ . The widths of the unscattered lines are  $W_0 = 54.7$  eV at  $\Theta = 0.02$  rad,  $W_0 = 35.9$  eV at  $\Theta = 0.01$  rad,  $W_0 = 29.6$  eV at  $\Theta = 0.003$  rad,  $W_0 = 29.5$  eV at  $\Theta = 0.0001$  rad.

$r_0, 10^{11}$ cm	$1-\zeta$		$W, \text{eV}$	
	$\Theta=0.02$ rad	$\Theta=0.01$ rad	$\Theta=0.02$ rad	$\Theta=0.01$ rad
5.0	0.93	0.93	59.2	40.3
3.2	0.91	0.91	61.1	40.9
1.8	0.88	0.86	62.3	41.8
0.8	0.82	0.78	64.5	43.7
0.4	0.65	0.58	68.3	45.3
$n_{e0}, 10^{14} \text{ cm}^{-3}$	$\Theta = 3 \times 10^{-3}$ rad	$\Theta = 10^{-4}$ rad	$\Theta = 3 \times 10^{-3}$ rad	$\Theta = 10^{-4}$ rad
1.0	0.86	0.82	30.9	31.1
4.0	0.71	0.66	31.8	32.0
16.0	0.49	0.45	32.9	33.0

$K_\alpha$  triplet, given that for the resonance line of the nickel triplet and  $K_\beta$  of iron  $\hat{\tau}_T > \tau_{cr}$  only for  $\alpha > 30$  and  $\alpha > 10$ , respectively (see Table 2).

Thus, the intensity “transfer” between the iron  $K_\beta$  line and the nickel  $K_\alpha$  triplet through resonant scattering turns out to be fairly likely. At the same time, the intensity of the entire set of lines does not undergo such a dramatic decrease as the iron  $K_\alpha$  triplet. However, this cannot completely explain the observed excess of radiation in this region relative to that expected from the FeXXV  $K_\alpha$  (6.7 keV) line under the assumption of solar elemental abundances.

Astro-H observations allow the nickel triplet lines and  $K_\beta$  of iron to be reliably resolved, thereby making it possible to determine the nickel abundance relative to iron in the jets of SS 433 *in situ*.

#### 5.1.4 S XV $K_\alpha$

The overall pattern typical of the  $K_\alpha$  triplets of helium-like ions at low energies (we will be interested primarily in sulfur and silicon; see Table 2) differs from that for high-energy triplets (e.g., of iron) in several respects. First, the triplet components have a large relative spectral separation ( $\Delta E/\Delta E_D$ ); as a result, the overlap and, hence, the interaction take place only for large  $\Theta \sim 0.02$  rad (see Fig. 8a). Nevertheless, we provide the attenuation coefficients  $1-\zeta$  for the entire triplet (see Table 7). Second,  $n_{e,crit} \propto Z^{13}$  turns out to be  $10^{14} \text{ cm}^{-3}$  (an accurate calculation for the corresponding temperature range was performed using the Cloudy 08.00 code). Therefore, for the fine structure of the triplets to be simulated in detail, the intensity redistribution of the forbidden and intercombination lines as a result of the collisional excitations from  $^3S_1$  (the upper level of the forbidden component) to  $^3P_{0,1,2}$  (the upper levels of the intercombination components) should be taken into account (Porquet et al. 2010). This redistribution is described in terms of their intensity ratio  $R(n_e) = z/(x+y) = \frac{r_0}{1+n_e/n_{e,crit}(T)}$ ,

where  $r_0$  is the value of this ratio in the low-density limit (from APEC), and the dependence  $n_{e,crit}(T)$  is obtained by fitting the Cloudy computation results.

Since Astro-H is inferior to Chandra HETGS in its spectral characteristics near the brightest lines of hydrogen- and helium-like sulfur and silicon, we omit the results of our analysis of the simulated spectra in the Astro-H resolution. For our analysis in the Chandra HEG resolution (Fig. 8a) we used, where possible, a model consisting of three Gaussians of the same FWHM with fixed centroids but with decoupled amplitudes  $w, x + y$ , and  $z$  for the resonance, intercombination, and forbidden components, respectively. Since the triplet components have different characteristics with respect to the scattering effects, one might expect these effects to affect noticeably the ratio  $R = z/(x + y)$  and the ratio  $G(T) = (z + x + y)/w$  of the total intensity of the forbidden and intercombination lines to the intensity of the resonance line, which is used to diagnose the plasma temperature (see, e.g., Porquet et al. (2010)). Given the importance of these ratios from the viewpoint of the physical interpretation of observational data, the summary table of results provides precisely the values of  $R$  and  $G$  (see Table 7).

For  $\Theta = 0.02$  rad the interaction between the triplet components resembles the situation with the  $K_\alpha$  triplet of helium-like iron at  $\Theta = 0.01$  rad, but complicated by the intensity redistribution of the forbidden and intercombination components. Therefore, we do not present the results of a detailed analysis for  $\Theta = 0.02$  rad, bearing in mind the impossibility of their clear and unambiguous interpretation.

For  $\Theta = 0.01$  rad, as a result of the rapid decrease in  $n_e \propto \xi^{-2}$  with increasing  $\xi$ , the effective optical depth for scattering by free electrons  $\hat{\tau}_T$  turns out to be greater than  $\tau_{cr}$  for the resonance photons only at  $r_0 = 4 \times 10^{10}$  cm, despite the large optical depth of the jet for resonant scattering in the allowed S XV triplet component (see Fig. 4). Therefore, the overall pattern is similar to that considered for the Ni XXVII  $K_\alpha$  triplet, i.e., the influence of scattering effects

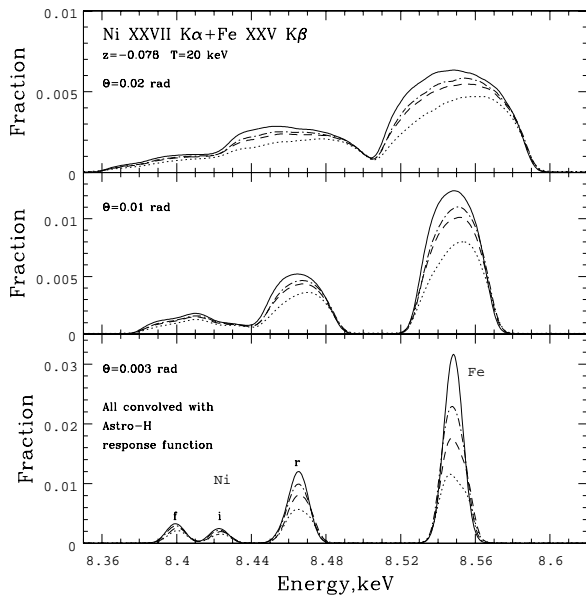


**Fig. 7.** Results of our simulations for the Ni XXVII  $K_\alpha$  and Fe XXV  $K_\beta$  for the approaching jet with  $T_0 = 20$  at a phase corresponding to  $z_b = -0.078$ . (a) The spectrum convolved with the Astro-H model response function for  $\Theta = 0.02$  rad; (b) the spectrum convolved with the Astro-H model response function for  $\Theta = 0.01$  rad; the dotted curve for  $r_0 = 4 \times 10^{10}$  cm, the curve with short dashes for  $r_0 = 8 \times 10^{10}$  cm, the dash-dotted curve for  $r_0 = 1.8 \times 10^{11}$  cm, and the solid curve indicates the unscattered line profile (the same for all  $r_0$ ); (c) the spectrum convolved with the Astro-H model response function for  $\Theta = 0.003$  rad; the dotted curve for  $n_{e0} = 1.6 \times 10^{15} \text{ cm}^{-3}$ , the curve with short dashes for  $n_{e0} = 4 \times 10^{14} \text{ cm}^{-3}$ , the dash-dotted curve for  $n_{e0} = 1.0 \times 10^{14} \text{ cm}^{-3}$ , and the solid curve indicates the unscattered line profile (the same for all  $n_{e0}$ ).

is small, the ratios  $R$  and  $G$  differ from their unscattered values  $R_0$  and  $G_0$  only slightly (see Table 7).

In the case of quasi-cylindrical models, the overall pattern of the spectra corresponds to that for the Fe XXV  $K_\alpha$  triplet (here,  $n_e$  changes little). As a result, the ratios  $R$  and  $G$  as well as the effective line width change noticeably. However, even in the case of an increase by a factor of 1.5–2, the line width for  $\Theta \leq 0.003$  rad remains considerably smaller than that at  $\Theta = 0.01$  (as distinct from the analogous situation for the FeXXV  $K_\alpha$  triplet).

### 5.1.5 Si XIII $K_\alpha$

The general scheme for analyzing and presenting the results for the  $K_\alpha$  triplet of helium-like silicon is completely identical to the scheme described in detail for the sulfur triplet in the preceding section. Therefore, here we omit the determination of the quantities given in Table 8. Similarly, the interpretation of the results of our analysis closely coincides with that for the sulfur triplet.

Nevertheless, an important distinctive feature of the silicon triplet is the possible influence of satellites on measured characteristics (e.g.,  $R$  and  $G$ ). We will defer a de-

tailed discussion of this question until Section 5.3.1, while for now note that the diagnostics of plasma parameters based on the ratios  $R$  and  $G$  can be strongly affected by the scattering effects. For example, an increase in these ratios (see Tables 7 and 8) as a result of scattering relative to the values corresponding to the optically thin approximation (Porquet et al. 2010) must lead to an underestimation of the density and temperature from observations.

Given the excellent spectral resolution of Chandra HETGS in this energy range, a detailed analysis of the line profiles corrected for the effects considered can provide information about the low-temperature part of the jet.

## 5.2 Broad Line Wings

Broad line wings are formed at a large number of photons that left the line due to their scattering by a free electron. The shape of these wings is well described by the single Compton scattering kernel with the application of relativistic corrections in the case of an isotropic radiation field defined by Eq. (19) from Sazonov, Sunyaev (2000). In this case, the only normalization is the quantity  $\zeta$ , i.e., the fraction of the photons that left the line, while the only parameter in fitting is the effective temperature of the scattering electrons  $T_e$ . This temperature reflects the contribution from various parts of the jet to the scattered radiation and, hence, allows the temperature and density profiles along the jet to be judged. For example, on average, higher-temperature fits correspond to the class of quasi-adiabatic models than to the class of quasi-cylindrical ones (see Fig. 9). This is due to a rapid decrease in density against the background of a slow change in temperature for the former and the directly opposite situation for the latter.

This single Compton scattering kernel has the following characteristic features: first, the presence of a cusp near  $E = E_0$  and, second, a noticeable asymmetry—the “right” (high-energy) wing is much broader than the “left” (low-energy) one. In addition, there is a probability of photon rescattering by an electron. However, at  $\hat{\tau}_T \sim 0.1$  the influence of rescatterings is negligible, with the possible exception of the far edges of the wings (see Fig. 9).

Since, in general, the broad wings of scattered lines are **always** present in the spectrum (the question is only in what quantities), an accurate measurement of their shape can be used as a universal (though model-dependent) tool for determining the jet parameters that is already accessible for present-day instruments. Undoubtedly, the contribution from the wings of neighboring lines slightly complicates the problem, but, at the same time, independent measurements in the high- and low-energy parts of the spectrum can reveal particular local features in the density and temperature distributions.

At the same time, it should be remembered that the continuum itself is also subject to scattering inside the jet, which is especially important for the photons in resonance with the electron transitions in ions. Nevertheless, our sim-

ulations with the addition of an appropriate wide continuum component showed that the continuum “subsidence” under the resonance lines for lines with significant equivalent widths affects only slightly the observed parameters of these lines ( $\lesssim 5\%$  for the intensity). Since a detailed discussion of the scattering effects on the continuum is beyond the scope of this paper, we will restrict ourselves here only to the remark made and will consider a number of effects affecting directly the lines.

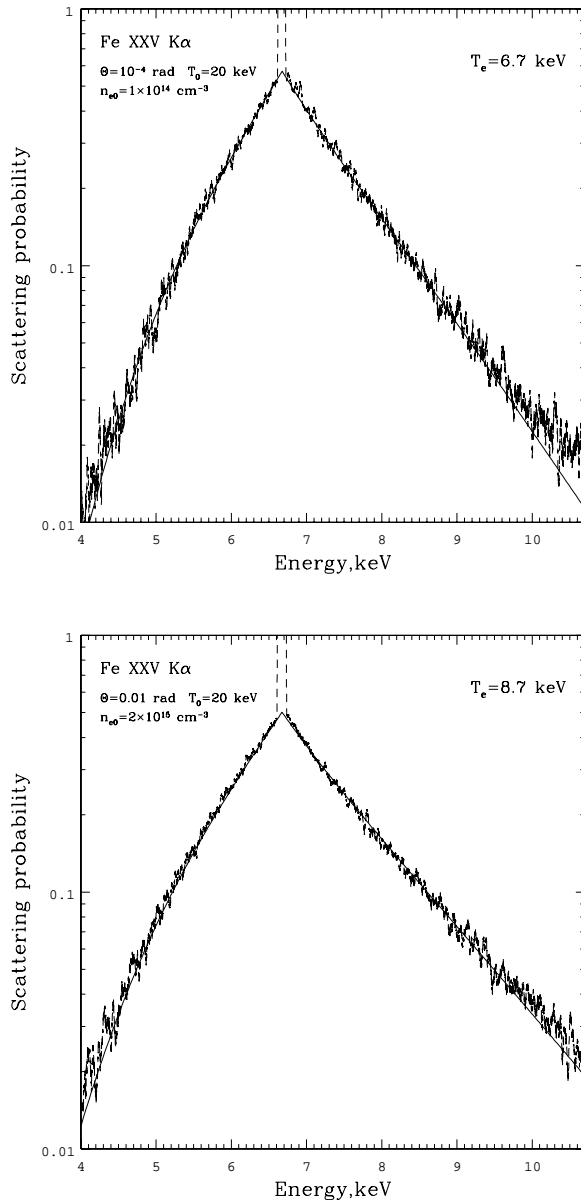


**Fig. 9.** Fitting the broad wings of the scattered FeXXV  $K\alpha$  line in the jet’s frame of reference by the single Compton electron scattering kernel from Sazonov, Sunyaev (2000) for one of the quasi-cylindrical models (top) and one of the quasi-adiabatic models (bottom). The photon scattering probability for a line with the central energy  $E_0 = 6.7$  keV and a cloud of electrons with temperature  $T_e$  is along the vertical axis.

**Table 6.** Analysis of the simulation results for the Ni XXVII  $K\alpha$  + Fe XXV  $K\beta$  in the Astro-H resolution for the approaching jet with  $T_0 = 20$  keV corresponding to  $z_b = -0.078$ . The widths of the unscattered lines are  $W_0 = 30.3$  eV at  $\Theta = 0.01$  rad,  $W_0 = 10.8$  eV at  $\Theta = 0.003$  rad,  $W_0 = 7.65$  eV at  $\Theta = 0.0001$  rad.

	$1-\zeta(\text{Ni})$	$1-\zeta(\text{Fe})$	$F(\text{Ni})/F(\text{Fe})$	$W, \text{eV}$
$r_0, 10^{11} \text{ cm}$	$\Theta = 0.01 \text{ rad}$			
5.0	0.94	0.94	0.61	30.3
3.2	0.92	0.92	0.61	30.6
1.8	0.89	0.89	0.61	30.9
0.8	0.84	0.83	0.61	31.3
0.4	0.71	0.65	0.65	31.3
$n_{e0}, 10^{14} \text{ cm}^{-3}$	$\Theta = 0.003 \text{ rad}$			
1	0.90	0.88	0.62	13.2
4	0.80	0.74	0.65	14.7
16	0.63	0.53	0.72	16.2
$n_{e0}, 10^{14} \text{ cm}^{-3}$	$\Theta = 0.0001 \text{ rad}$			
1	0.87	0.83	0.64	11.2
4	0.77	0.68	0.70	12.6
16	0.60	0.48	0.77	14.1

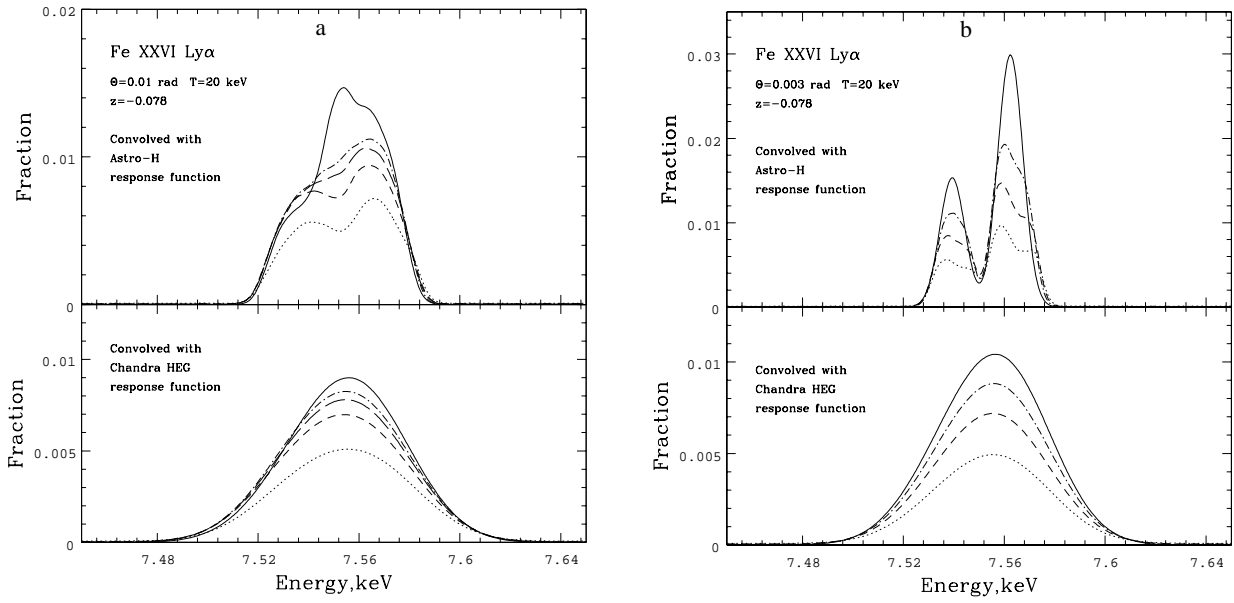


**Fig. 6.** Results of our simulations for the FeXXVI  $Ly\alpha$  doublet for the approaching jet with  $T_0 = 20$  keV at a phase corresponding to  $z_b = -0.078$ . (a)  $\Theta = 0.01$ ; the upper panel shows the spectrum convolved with the Astro-H model response function; the lower panel shows the spectrum convolved with the Chandra HEG model response function; the dotted curve for  $r_0 = 4 \times 10^{10}$  cm, the curve with short dashes for  $r_0 = 8 \times 10^{10}$  cm, the curve with long dashes for  $r_0 = 1.8 \times 10^{11}$  cm, the dash-dotted curve for  $r_0 = 3.2 \times 10^{11}$  cm, and the solid curve indicates the unscattered line profile (the same for all  $r_0$ ). (b)  $\Theta = 0.003$  rad; the upper panel shows the spectrum convolved with the Astro-H model response function; the lower panel shows the spectrum convolved with the Chandra HEG model response function; the dotted curve for  $n_{e0} = 1.6 \times 10^{15} \text{ cm}^{-3}$ , the curve with short dashes for  $n_{e0} = 4 \times 10^{14} \text{ cm}^{-3}$ , the dash-dotted curve for  $n_{e0} = 1.0 \times 10^{14} \text{ cm}^{-3}$ , and the solid curve indicates the unscattered line profile (the same for all  $n_{e0}$ )

**Table 7.** Analysis of the simulation results for the SXV  $K\alpha$  triplet in the Chandra resolution for the approaching jet with  $T_0 = 20$  keV at a phase corresponding to  $z_b = -0.078$

	$1-\zeta$	R ( $R_0$ )	G ( $G_0$ )	W ( $W_0$ ), eV
$r_0, 10^{11} \text{ cm}$	$\Theta = 0.01 \text{ rad}$			
5.0	0.97	1.98 ( 1.92 )	0.65 ( 0.64 )	8.92 ( 8.77 )
3.2	0.96	1.98 ( 1.92 )	0.65 ( 0.64 )	8.96 ( 8.77 )
1.8	0.93	1.91 ( 1.92 )	0.65 ( 0.64 )	9.06 ( 8.77 )
0.8	0.88	1.58 ( 1.62 )	0.65 ( 0.64 )	9.09 ( 8.77 )
0.4	0.71	0.71 ( 0.73 )	0.67 ( 0.64 )	8.97 ( 8.77 )
$n_{e0}, 10^{14} \text{ cm}^{-3}$	$\Theta = 0.003 \text{ rad}$			
1	0.90	1.87 ( 1.87 )	0.64 ( 0.59 )	3.57 ( 2.85 )
4	0.75	1.39 ( 1.34 )	0.69 ( 0.59 )	3.83 ( 2.85 )
16	0.55	0.66 ( 0.57 )	0.76 ( 0.59 )	4.16 ( 2.85 )
$n_{e0}, 10^{14} \text{ cm}^{-3}$	$\Theta = 0.0001 \text{ rad}$			
1	0.80	1.75 ( 1.71 )	0.71 ( 0.59 )	2.93 ( 1.73 )
4	0.65	1.26 ( 1.14 )	0.81 ( 0.59 )	3.25 ( 1.73 )
16	0.46	0.62 ( 0.49 )	0.90 ( 0.59 )	3.52 ( 1.73 )

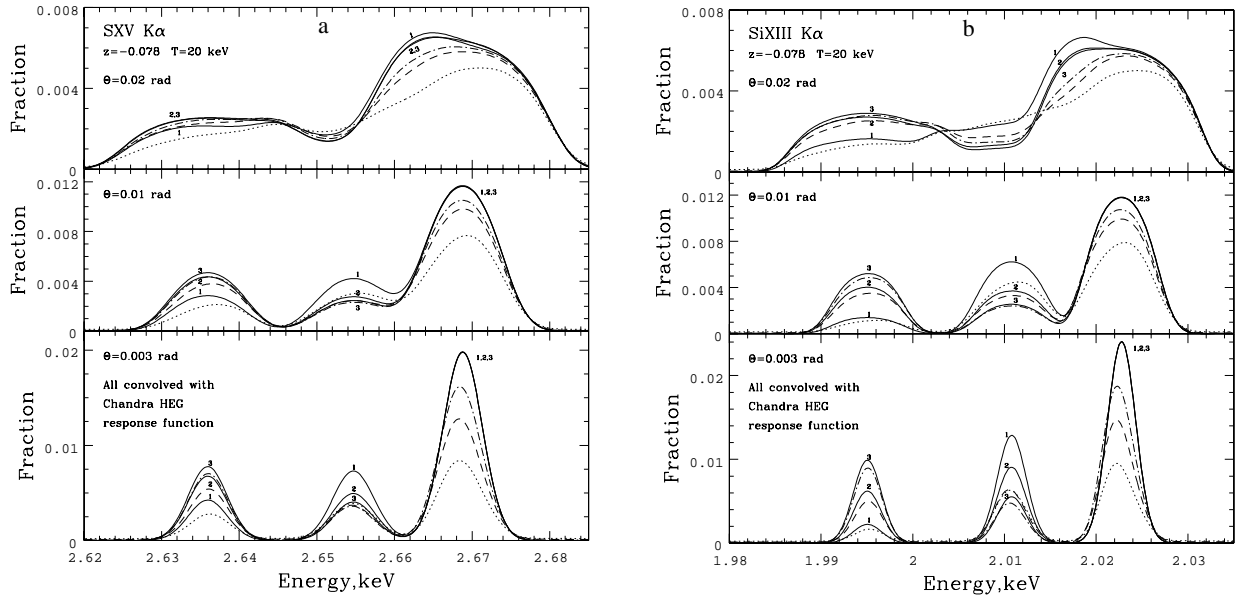


**Fig. 8.** Results of our simulations for the SXV  $K_{\alpha}$  triplet (a) and the SiXIII  $K_{\alpha}$  triplet (b) for the approaching jet with  $T_0 = 20$  keV at a phase corresponding to  $z_b = -0.078$ . The upper panel:  $\Theta = 0.02$  rad; the spectrum convolved with the Chandra HEG model response function; the dotted curve for  $r_0 = 4 \times 10^{10}$  cm, the curve with short dashes for  $r_0 = 8 \times 10^{10}$  cm, the dash-dotted curve for  $r_0 = 1.8 \times 10^{11}$  cm, 1, 2, 3 represent the unscattered line profile for  $r_0 = 4 \times 10^{10}$  cm,  $r_0 = 8 \times 10^{10}$  cm, and  $r_0 = 1.8 \times 10^{11}$  cm, respectively. The middle panel:  $\Theta = 0.01$  rad; the spectrum convolved with the Chandra HEG model response function; the dotted curve for  $r_0 = 4 \times 10^{10}$  cm, the curve with short dashes for  $r_0 = 8 \times 10^{10}$  cm, the dash-dotted curve for  $r_0 = 1.8 \times 10^{11}$  cm, 1, 2, 3 represent the unscattered line profile for  $r_0 = 4 \times 10^{10}$  cm,  $r_0 = 8 \times 10^{10}$  cm, and  $r_0 = 1.8 \times 10^{11}$  cm, respectively. The lower panel:  $\Theta = 0.003$  rad; the spectrum convolved with the Chandra HEG model response function; the dotted curve for  $n_{e0} = 1 \times 10^{14}$  cm $^{-3}$ , the curve with short dashes for  $n_{e0} = 4 \times 10^{14}$  cm $^{-3}$ , the dash-dotted curve for  $n_{e0} = 1.6 \times 10^{15}$  cm $^{-3}$ , 1, 2, 3 represent the unscattered line profile for  $n_{e0} = 1.6 \times 10^{15}$  cm $^{-3}$ ,  $n_{e0} = 4 \times 10^{14}$  cm $^{-3}$ , and  $n_{e0} = 1 \times 10^{14}$  cm $^{-3}$ , respectively.

**Table 8.** Analysis of the simulation results for the SiXIII  $K_{\alpha}$  triplet in the Chandra resolution for the approaching jet with  $T_0 = 20$  keV at a phase corresponding to  $z_b = -0.078$

	$1-\zeta$	$R (R_0)$	$G (G_0)$	$W (W_0)$ , eV
$r_0, 10^{11}$ cm				
$\Theta = 0.01$ rad				
5.0	0.98	2.33 (2.33)	0.720 (0.713)	6.90 (6.76)
3.2	0.96	2.25 (2.27)	0.716 (0.709)	6.92 (6.75)
1.8	0.94	1.95 (1.98)	0.709 (0.699)	6.91 (6.71)
0.8	0.89	1.09 (1.10)	0.706 (0.691)	6.93 (6.67)
0.4	0.72	0.26 (0.26)	0.708 (0.671)	6.68 (6.56)
$n_{e0}, 10^{14}$ cm $^{-3}$				
$\Theta = 0.003$ rad				
1	0.90	1.79 (1.76)	0.70 (0.64)	2.63 (2.08)
4	0.76	0.73 (0.67)	0.74 (0.64)	2.80 (2.08)
16	0.55	0.22 (0.17)	0.79 (0.64)	2.96 (2.08)
$n_{e0}, 10^{14}$ cm $^{-3}$				
$\Theta = 0.0001$ rad				
1	0.78	1.38 (1.24)	0.81 (0.63)	2.26 (1.15)
4	0.63	0.61 (0.48)	0.89 (0.63)	2.51 (1.15)
16	0.45	0.21 (0.14)	0.91 (0.63)	2.68 (1.15)



### 5.3 The Influence of Other Effects

Apart from the scattering inside the jet, there are also several effects capable of affecting the observational line characteristics (intensity, width, etc.) and the line ratios used to diagnose the plasma parameters. In this Section, we estimate the possible effects of satellites of bright lines, nutations, and photoionization and photoexcitation.

#### 5.3.1 Satellites and the Overlap of Close Lines

On the one hand, the presence of satellites near bright lines slightly complicates the analysis and interpretation of the spectra, but, on the other hand, investigating the satellite parameters (provided an appropriate spectral resolution of the instrument) is a powerful tool for diagnosing the parameters of the emitting medium *per se* (see, e.g., Porquet et al. (2010)).

For the triplets of helium-like ions, the bulk of the satellite intensity integrated over the entire jet is concentrated in about 25 lines inside the triplet, i.e., between the forbidden and resonance lines. In this case, the satellite intensity relative to the resonance line slightly increases with increasing charge of the ion nucleus  $Z$ . For example, the contribution of the satellites in the jet model under consideration for sulfur ( $Z = 16$ ) is about 12% of the intensity of the  $K_\alpha$  triplet of the helium-like ion and about 20% for the same triplet of iron ( $Z = 26$ ). At the same time, there can be cases where the energies of the bright lines corresponding to the transitions in various ions of the same or different elements are close. In particular, such a situation takes place for the forbidden line of the helium-like silicon  $K_\alpha$  triplet coincident with the MgXII  $Ly_\gamma$  doublet. As a result, not only the normalization of the ratios  $R$  and  $G$  (see Section 5.1.4) but also the shape of the temperature dependence  $G(T)$  itself changes (see Fig. 10a).

In the case of intrinsically broad lines, the satellites cannot be resolved in principle, but their contribution to the total intensity of the blend and its width can be substantial. For example, for the triplet of helium-like iron, the effective increase in the width  $W$  of the blend components (for a definition of  $W$ , see Section 5.1.1) due to the contribution of satellites turns out to be  $\Delta W \gtrsim 1$  eV, i.e.,  $\gtrsim 5\%$  at  $\Theta = 0.01$  rad (see Fig. 10b).

#### 5.3.2 Nutations

The nutation and, possibly, jitter of the jets (Kubota et al. 2010) are other factors contributing to the broadening of the observed lines. To estimate the nutation broadening, we used the model of ephemerides (Katz 1987) with the parameters found by Gies et al. (2002) that defines  $z$  for each of the jets at an arbitrary instant of time. The influence on the line width can be described in terms of the total change  $\Delta z$  in some time interval  $(t_0, t_0 + t_{obs})$  short compared to the nutation period (6.28 days), where  $t_0$  is the

**Table 9.** Nutation broadening of the Fe XXV (6.70 keV) and Si XIII (1.86 keV) lines for phases corresponding to the Chandra observations, a report on which is contained in Marshall et al. (2002) [1], Namiki et al. (2003) [2], and Lopez et al. (2006) [3].

Report	$z_b$	$t_{obs}$ , ks	$\Delta z, 10^{-4}$	$\delta E_0$ , eV	
				Fe	Si
[1]	-0.078	32.0	5	8	2.2
[2]	0.046	21.3	9	11	3.1
[3]	0.014	25.7	10	13	3.6

starting time of observations and  $t_{obs}$  is their total duration. For example, for  $t_{obs} = 20$  ks, the maximum value of  $\Delta z$  is about 0.0024, which is in good agreement with the measured maximum nutation variability  $dz/dt \approx 0.004$  in 0.33 day (Fabrika 2004). In this case, as long as the total time of observations is much shorter than the nutation period (6.28 days),  $\Delta z$  scales linearly in  $t_{obs}$  with a good accuracy. The change in the energy  $E_0$  of the line centroid due to nutation can be estimated as  $\delta E_0 = \frac{E_0}{(1+z)^2} \Delta z$ . The full width at half maximum of the line with nutation is then

$$FWHM_n \approx \sqrt{FWHM^2 + \frac{2\ln 2}{3} \delta E_0^2}, \quad (24)$$

where  $FWHM$  is the full width at half maximum without nutations. The values of  $\Delta z$  and  $\delta E_0$  for the Fe XXV (6.7 keV) and Si XIII (1.86 keV) lines of the “blue” jet for specific values of  $t_0$  and  $t_{obs}$  corresponding to the Chandra observations are given in Table 9.

Given the observed line widths, it follows from relation (24) that the nutation broadening can serve as an additional ( $\sim 5\%$ ) correction to the FWHM.

#### 5.3.3 Photoionization and photoexcitation

So far our analysis was based on the assumption that the atoms in the plasma of the jets in SS 433 were ionized and excited exclusively by collisions with electrons; in this case, the influence of the electromagnetic radiation fields permeating the jets is negligible. How valid is this assumption?

As regards the intrinsic X-ray radiation from the jets, it should not affect significantly the ionization balance of the hot plasma, because the jets are optically thin for the ionizing continuum. However, the gas of the relativistic jets in SS 433 can be irradiated by the much more intense X-ray radiation produced inside the funnel of a thick accretion disk near the black hole (Fabrika 2004). Indeed, if SS 433 is similar to the ultraluminous X-ray sources observed in nearby galaxies (Roberts 2007) but only turned to us by its edge rather than by the accretion disk plane, then the X-ray luminosity emitted within the funnels can be  $L_x \sim 10^{40} - 10^{41}$  erg/s (when recalculated to an isotropic source). The photoionization fraction of the jet gas in the field of such radiation will be determined by the ion-

ization parameter  $\xi = L/nr^2$  and, depending on the density  $n$  and the distance to the jet base  $r$ , can reach  $10^3$  or even greater values. In this case, the influence of photoionization on the ionization balance in the hot plasma of the jets can be significant (e.g., Kallman, McCray (1982)). However, Chandra HETGS measurements (Marshall et al. 2002) showed that the permitted line dominates in the resolved (in energy)  $K\alpha$  triplets, primarily of SiXIII. This means that collisions dominate over photoionization in the formation region of these lines. Since the ionization parameter  $\xi = L/nr^2$  does not change greatly along the X-ray jet for both quasi-adiabatic and quasi-cylindrical models, collisions dominate over photoionization during the excitation of levels in the atoms of heavier elements as well. Nevertheless, we are going to consider in more detail the influence of X-ray radiation from the inner accretion disk regions on the ionization and radiative properties of the plasma in the jets of SS 433 in a future paper.

The supercritical accretion disk in SS 433 is also a powerful source of ultraviolet radiation with a characteristic temperature of  $\sim 50000$  K and a luminosity of  $\sim 10^{40}$  erg/s (Dolan et al. 1997). This is also confirmed by observations of the radio nebula W50 produced by the impact of the jets in SS 433 on the interstellar medium (Fabrika 2004). An ultraviolet photon of appropriate energy can excite the electron from the upper level ( $^3S$ ) of the forbidden transition in a helium-like ion to the upper level ( $^3P$ ) of the intercombination transition (Porquet et al. 2001). In a strong ultraviolet radiation field, this effect leads to a redistribution of the radiation fluxes in the forbidden and intercombination lines of the triplets in favor of the latter, i.e., to a decrease in ratio  $R$ , just as in the case of a high gas density. This is particularly true for the lighter elements. Calculations (Porquet et al. 2001) (and our Cloudy computations) for a blackbody radiation field with a temperature of  $50\,000$  K show that the effect for the SiXIII triplet must be significant even if the dilution of radiation related to the fact that the disk radiation permeates the jets from some distance and at some angle is taken into account. Since there is a considerable uncertainty in determining the characteristic temperature and the geometry of the ultraviolet radiation source (Gies et al. 2002), we will restrict ourselves here only to the above remark of a somewhat qualitative character.

## 6 COMPARISON WITH OBSERVATIONS

In this part, we would like to discuss the application of our simulation results to analyzing and interpreting the Chandra spectra of SS 433 at the phase of the greatest disk opening toward the observer (Marshall et al. 2002). The weighted mean line width in these observations corresponded to the scenario of a ballistic flow with an opening angle  $\Theta = 0.^\circ 61 \pm 0.^\circ 03 \approx 0.01$  rad. The jet density  $n_e \sim 10^{14} \text{ cm}^{-3}$  in the line formation region ( $T \sim 1$  keV) was estimated from the SiXIII  $K_\alpha$  triplet. The physical volume of this region, hence, the distance of this region from

the cone apex (assuming a conical flow with an opening angle  $\Theta$ ) was estimated from the emission measure of the component with such a temperature in a four-temperature model describing satisfactorily the line intensities. Using the estimates of the emission measure for the other three components and assuming the temperature profile to be adiabatic, the corresponding locations and densities of these components were found. As a result, a physical picture was obtained that provided satisfactory agreement with the observed spectrum but, at the same time, had significant shortcomings. Below, we would like to show how this picture changes if the scattering effects we considered and others (see the “Results” Section) are taken into account. Since the triplets of helium-like iron (FeXXV  $K_\alpha$ ) and silicon (SiXIII  $K_\alpha$ ) were the main diagnostic tools, we will dwell on a comparison of the measured line characteristics with the results of our calculations.

As has already been noted above, the Chandra HETGS spectral resolution ( $\sim 200@6.7$  keV) is insufficient for investigating the fine structure of the FeXXV  $K_\alpha$  triplet ( $\sim 300@6.7$  keV is needed). Therefore, when the observed profile is analyzed, some fixed ratios of the components ( $f/r$  and  $i/r$ ) is assumed (e.g.,  $f/r = 0.23$  and  $i/r = 0.28$  in Namiki et al. (2003)). Figures 11a and 11d show how strongly these ratios are subjected to the scattering effects, which points to the necessity of correcting the line widths estimated within a simple model. An unresolvable triplet with enhanced (compared to the resonance line) forbidden and intercombination components can appear as consisting of broader components with a bright resonance line but with a shifted centroid. Bearing in mind the broadening by scattering (Fig. 11b) and the additional possibilities for broadening from the “Results” Section, it should be recognized that the models with  $\Theta < 0.01$  rad are admissible from the viewpoint of observations in the high-energy part of the spectrum. In addition, the decrease in triplet intensity (Fig. 11a) due to the light scattering effects implies that the emission measure of the hottest parts of the jet estimated from the observed iron line intensities and the heavy-element abundances estimated from the ratio of the observed intensities of the corresponding lines should be corrected significantly. Thus, the scattering effects affect significantly the jet parameters ( $\Theta, n_{e0}, r_0$ ) estimated from the FeXXV  $K_\alpha$  triplet characteristics in Chandra observations.

In contrast, the remarkable spectral characteristics of the Chandra instruments in the low-energy region allow the fine structure of the helium-like silicon triplet (and, to some extent, the SXV  $K_\alpha$  triplet) to be investigated, but, at the same time, they also require a more detailed study of their formation mechanisms for interpreting the observed line characteristics. The observed width of the SiXIII  $K_\alpha$  triplet components (FWHM  $\approx 1900$  km/s) corresponds to a jet opening angle  $\Theta \simeq 0.015$  rad\*. This makes the inter-

\* It is worth noting that in Marshall et al. (2002) the weighted mean

pretation of the widths in terms of quasi-cylindrical models very problematic, even if the possible broadening effects we considered are taken into account (Fig. 12b). Thus, the models with  $\Theta \geq 0.01$  rad are much more preferential. However, the intensity of the SiXIII  $K_\alpha$  triplet decreases significantly as a result of scatterings even in this case (Fig. 12a). This implies the necessity of a significant correction of the estimated emission measure for the jet region with  $T \sim 1$  keV, though slightly less significant than that for the hotter region at the jet base.

Figures 12c and 12d present the ratios  $R$  and  $G$  for the silicon triplet derived in our calculations by taking into account the scattering effects and the contribution from the MgXII  $L_{\gamma\gamma}$  doublet, whose energy almost coincides with the energy of the forbidden silicon line (see also Section 5.3.1). These results of our calculations are compared with the ratios (confidence intervals)  $R$  and  $G$  measured by Marshall et al. (2002):  $R = 1.18 \pm 0.26$  and  $G = 0.92 \pm 0.13$ . The following conclusions can be drawn from this comparison. First, the measured value of  $G$  is consistent with most of the quasi-adiabatic and quasi-cylindrical jet models considered. Second, the measured value of  $R$  points to  $r_0 \Theta \sim 10^9$  cm, which together with  $\Theta \simeq 0.01$  rad estimated from the line broadening gives  $r_0 \sim 10^{11}$  cm. This is consistent with the estimates from Medvedev, Fabrika (2010) but exceeds appreciably the value obtained by Marshall et al. (2002)-  $r_0 \sim 2 \times 10^{10}$  cm, and, at the same time, is less than  $r_0 \sim 10^{12}$  cm found by Filippova et al. (2006) from the eclipse of the jets by the optical companion.

The presented comparison of the results of our numerical calculations with the results of observations published by Marshall et al. (2002) is more likely qualitative than quantitative in nature. Obviously, comparison of the spectral predictions of our model for the scattering of radiation in the jets of SS 433 directly with the Chandra HETGS data (Marshall et al. 2002) is required to formulate more reliable conclusions. However, this is beyond the scope of our paper.

## 7 CONCLUSIONS

Let us briefly list our main conclusions:

(1) The effect of a decrease in line intensity due to scattering inside the jet turns out to be very pronounced, but it does not exceed 60% in magnitude on the entire grid of parameters. Thus, such anomalies as the excess of radiation in the region of the helium-like nickel triplet are difficult to explain in terms of the scattering effects alone, it is quite possible to make the problem less dramatic. At the same time, diagnosing the jet plasma parameters based on the line intensity ratios turns out to be impossible without allowance for the scattering effects, because the introduced shift can lead to significant systematic errors.

width FWHM  $\approx 1710$  km/s measured from all lines corresponds to an opening angle  $\Theta \approx 0.^\circ 77 \approx 0.014$  rad (which is easy to see from Eqs. (3) and (4) of this paper), while the authors provide  $\Theta \approx 0.^\circ 61 \approx 0.01$  rad.

(2) The scattering inside the jets, along with the nutational motion and the contribution of satellites, lead to a noticeable additional line broadening. This can lead to overestimates of the opening angle  $\Theta$  from the line width in Chandra X-ray observations. As a consequence, the models with  $\Theta \sim 0.005 - 0.01$  rad remain admissible. Therefore, it is worth noting that the more complex scenario of a nonconical relativistic flow (for example, ongoing collimation; Namiki et al. (2003)), which can be described by the change in  $\Theta$  along the jet in some approximation, may actually be realized.

(3) There must be broad wings of scattered radiation near the brightest lines, distorting the shape of the continuum in a certain way. The magnitude of this distortions turns out to be of the order of (or even greater than) the contribution from the recombination and two-photon components. As an illustration, we provide a synthetic broadband spectrum of the approaching jet at a phase corresponding to the Chandra X-ray observations of SS 433 in 1999 at a distance of 5 kpc (Marshall et al. 2002) (Fig. 13). Accurately measuring the shape of the scattered component can give additional information about the density distribution and the temperature profile along the jet.

(4) The fine structure of the lines is very sensitive to the scattering effects (especially in the case of doublets and triplets). This makes its investigation a powerful tool for diagnosing the jet parameters – the density of the emitting region (and, consequently, its size) and the opening angle  $\Theta$ . New-generation X-ray observatories (primarily Astro-H) equipped with spectrometers with a resolution of several electronvolts (microcalorimeters) will allow one to quickly (in an exposure time of 10 ks, Astro-H will be able to collect  $\sim 600$  photons in the FeXXV (6.7 keV) line and, consequently,  $\sim 60$  photons in the broad wings) get a clear idea of the mechanisms for the formation of X-ray lines in the spectrum of the jets in SS 433.

## ACKNOWLEDGMENTS

This work was supported by Programs P-21 and OFN-16 of the Russian Academy of Sciences and the Program for Support of Leading Scientific Schools of the Russian Federation (NSH-5069.2010.2).

## REFERENCES

2. Brinkmann, W., Kotani, T. & Kawai, N. 2005, A & A, 431, 575
3. Cherepashchuk A. M., Sunyaev R. A., Fabrika S. N., Postnov K. A., Molkov S. V., Barsukova E. A., Antokhina E. A., Irmambetova T. R., Panchenko I. E., Seifina E. V., Shakura N. I., Timokhin A. N., Bikmaev I. F., Sakhibullin N. A., Aslan Z., Khamitov I., Pramsky A. G., Sholukhova O., Gnedin Yu. N., Arkharov A. A., Larionov V. M. *Astron. Astrophys.* **437**, 561 (2005)
4. Dolan J. F., Boyd P. T., Fabrika S., et al. *Astron. Astrophys.* **327**, 648 (1997)
5. Fabrika S. 2004, *ASPRv*, 12, 1
6. Ferland G. J., Korista K. T., Verner D. A., Ferguson J. W., Kingdon J. B., Verner E. M. 1998, *PASP*, 110, 761
7. Filippova, E., Revnivtsev, M., Fabrika, S., Postnov, K. & Seifina, E., 2006, A & A 460, 125-131
8. Gies, D. R., Huang, W., & McSwain, M. V. 2002, *ApJ*, 578, L67
9. Hamilton, D. R. 1947, *ApJ*, 106, 457
10. Kallman, T. R. & McCray, R. 1982, *ApJS*, 50, 263
11. Katz J. I. 1987, *ApJ*, 317, 264
12. Kotani, T., Kawai, N., Matsuoka, M., & Brinkmann, W. 1996, *PASJ*, 48, 619
13. Kubota, K., Ueda, Yo., Kawai, N., Kotani, T., Namiki, M., Kinugasa, K., Ozaki, S., Iijima, T., Fabrika, S. 2010, *PASJ*, 62, 323
14. Lodders, K. 2003, *Astrophys. J.*, 691, 1220
15. Lopez, L. A., Marshall, H. L., Canizares, C. R., Schulz, N. S., Kane, J. F. 2006, *ApJ*, 650, 338
16. Marshall, H. L., Canizares, C. R. & Schulz, N. S. 2002, *ApJ*, 564, 941
17. Medvedev, A., Fabrika, S. 2010, *MNRAS*, 402, 479
18. Mewe, R., Schrijver, J. 1978a, *AAP*, 65, 99
19. Namiki M., Kawai N., Kotani T. & Makishima K. 2003, *PASJ*, 55, 281
20. Porquet, D., Dubau, J. 2000, *AAP*, 143, 495
21. Porquet, D., Mewe, R., Dubau, J., Raassen, A. J. J., & Kaastra, J. S. 2001, *Astron. Astrophys.*, 376, 1113
22. Porquet, D., Dubau, J., Grosso, N. 2010, *SSR.*, 157, 103
23. Pozdnyakov, L. A., Sobol, I. M., Sunyaev, R. A. 1983, *ASPRv*, 2, 189
24. Roberts, T. P. 2007, *Ap & SS*, 311, 203
25. Sazonov, S. Yu., Sunyaev, R. A. 2000, *ApJ*, 543, 28
26. Sazonov, S. Yu., Churazov, E. M., Sunyaev, R. A. 2002, *MNRAS*, 333, 191
27. Smith, R. K., Brickhouse, N. S., Liedahl, D. A., Raymond, J. C. 2001, *ApJ*, 556, L91
28. Sobol', I. M., *Numerical Monte-Carlo Methods* (Nauka, Moscow, 1973), p. 221 [in Russian]
29. Takahashi, T., Mitsuda, K., Kelley, R. et al. 2010, *SPIE*, 7732, 27
30. Zhuravleva, I. V., Churazov, E. M., Sazonov, S. Yu., Sunyaev, R. A., Forman W., Dolag K. 2010, *MNRAS*, 403, 129

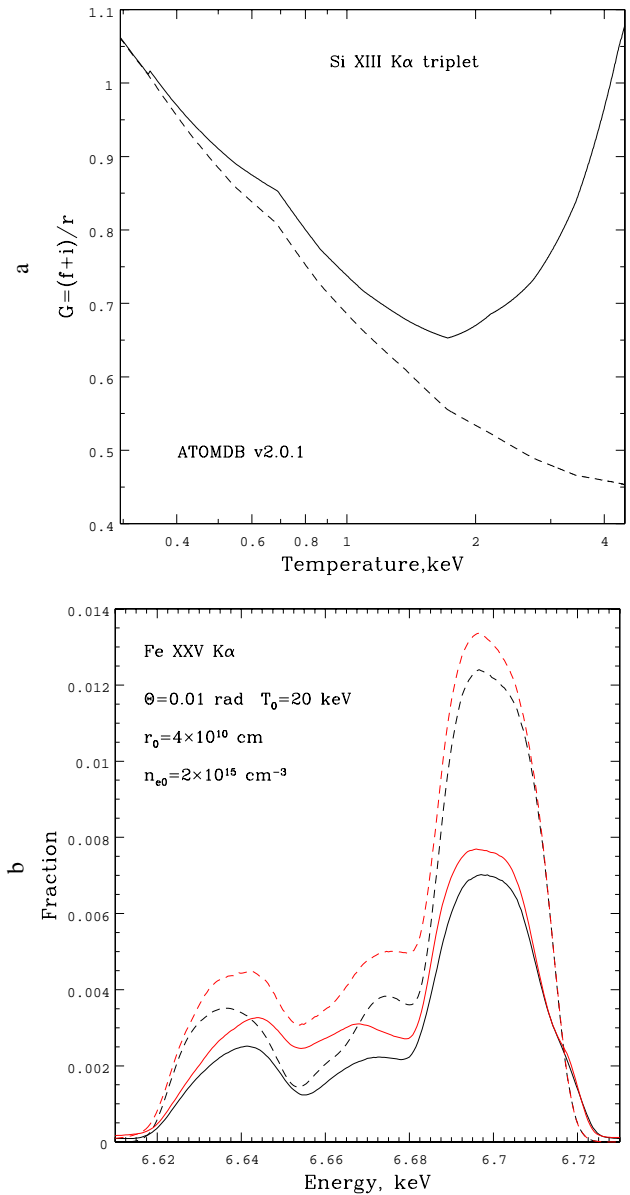


**Fig. 10.** (a) Influence of the Mg XII  $L\gamma$  line on the ratio  $G = (f + i)/r$  in the Si XIII  $K\alpha$  triplet: the solid and dashed curves are for the cases with and without Mg XII  $L\gamma$ , respectively. The computation was performed using ATOMDB v2.0.1. (b) The contribution from the satellites of the Fe XXV  $K\alpha$  triplet to the radiation intensity at 6.7 keV: the dashed and solid curves are for the cases without and with scattering, respectively; red—with satellites, black—without satellites.

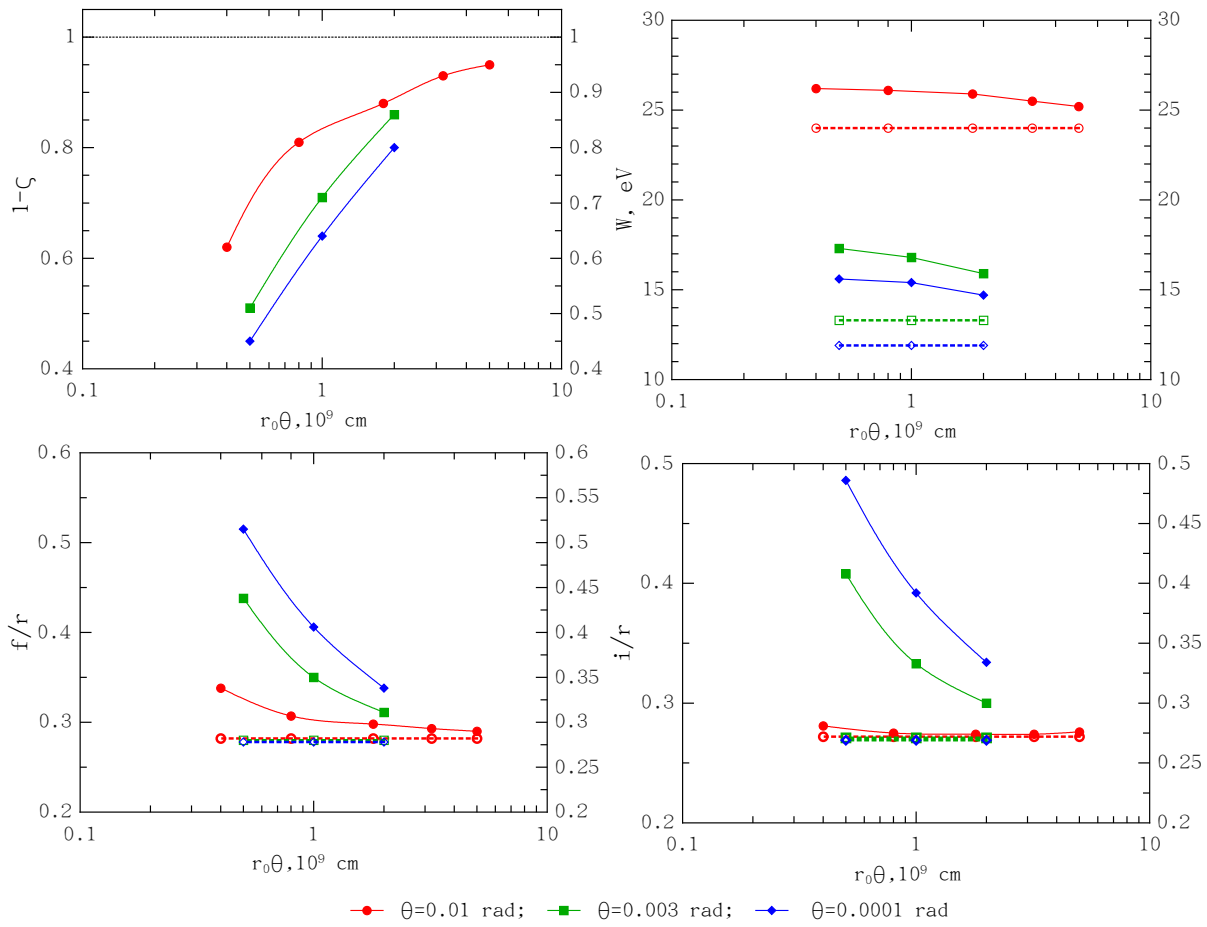


**Fig. 11.** Analysis of the simulation results for the FeXXV  $K_{\alpha}$  triplet in the Chandra HEG resolution for the approaching jet with  $T_0 = 20$  keV at the phase of the greatest disk opening toward the observer. The dashed lines (with the corresponding open symbols) correspond to the unscattered line characteristics.

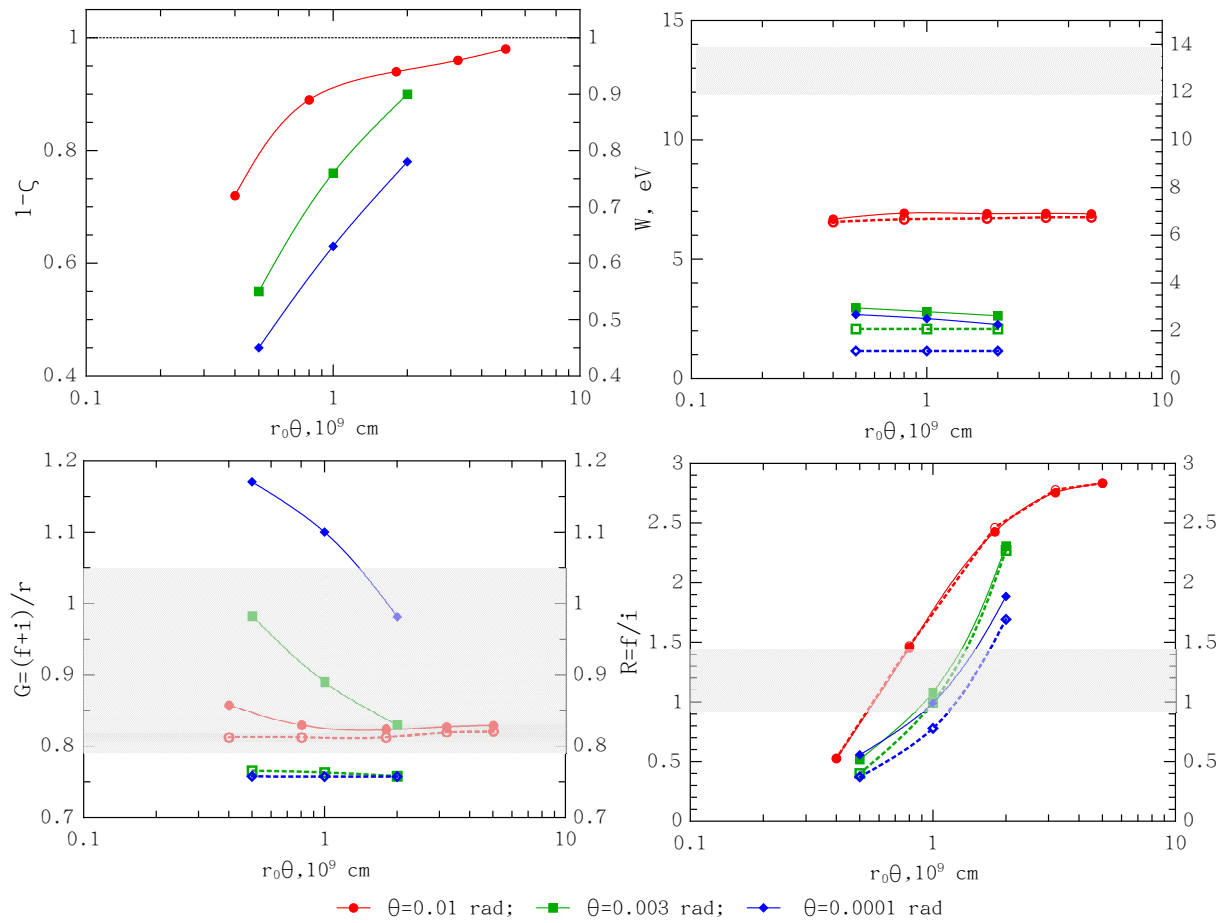


**Fig. 12.** Analysis of our simulation results for the SiXIII  $K_\alpha$  triplet in the Chandra HEG resolution for the approaching jet with  $T_0 = 20$  keV at the phase of the greatest disk opening to the observer. The dashed lines (with the corresponding open symbols) correspond to the unscattered line characteristics. The ratios  $R$  and  $G$  are presented by taking into account the contribution from the MgXII  $L\gamma_\gamma$  doublet. The shaded regions correspond to  $R$  and  $G$  measured in Chandra observations (Marshall et al. 2002).

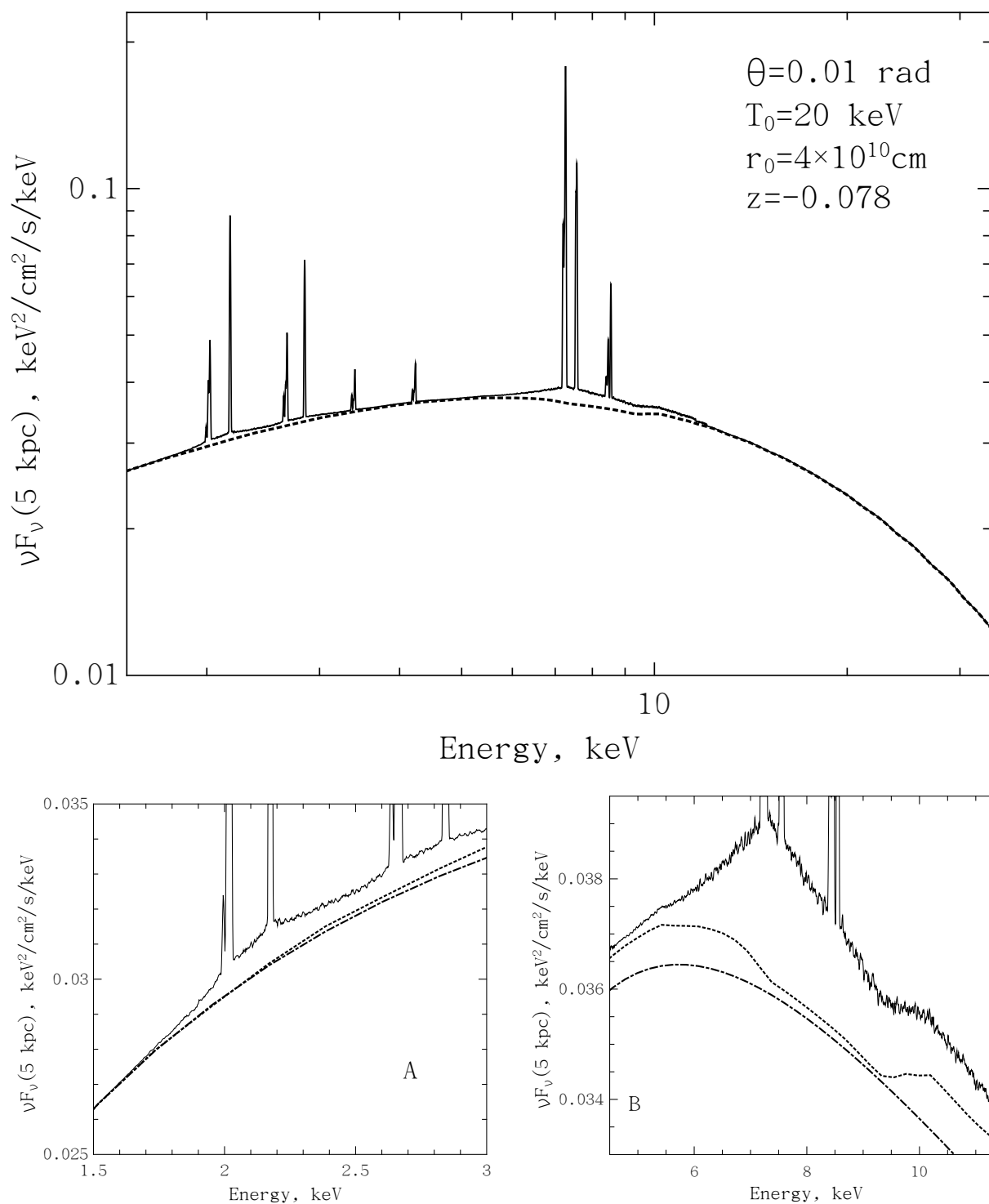


**Fig. 13.** Broadband simulated synthetic spectrum (solid line) of the approaching jet ( $z = -0.078$ ) at a distance of 5 kpc. The continuum radiation (dashed line) was computed using ATOMDB v2.0.1 (the NoLine model). All of the lines from Table 1 with allowance made for their scattering inside the jet but without allowance for the contribution of satellites were included. Magnified fragments of the broadband spectrum in the low-energy (bottom left) and high-energy (bottom right) regions. The dash-dotted line indicates the contribution from bremsstrahlung (the *brems* model in XSPEC v12.6.0). The difference between the bremsstrahlung and NoLine continua is due to the presence of recombination and two-photon components.